Rashid M, Horrocks BR, Healy N, Goss JP, Horsfall AB.

Optical properties of mesoporous 4H-SiC prepared by anodic electrochemical etching.

***Journal of Applied Physics* 2016, 120(19), 194303.**

Optical Properties of Mesoporous 4H-SiC Prepared by Anodic Electrochemical Etching

Marzaini Rashid[1) 2)], B.R.Horrocks[3)], N.Healy[1)], J.P. Goss[1)], A.B. Horsfall[1)]
[1)]School of Electrical and Electronic Engineering, Newcastle University, Newcastle Upon Tyne, NE1 7RU, UK
[2)]School of Physics, Universiti Sains Malaysia, 11800 USM, Penang, Malaysia
[3)]School of Chemistry, Newcastle University, Newcastle Upon Tyne, NE1 7RU, UK

E-mail: m.m.b.m.rashid@newcastle.ac.uk

Abstract

Porous silicon carbide was fabricated from *n*-type 4H-SiC substrates via anodic electrochemical etching in HF/ethanol solution and suspended in ethanol after ultrasonication. We observed three photoluminescence bands; those at wavelengths of 303 nm and 345 nm were above the bulk bandgap and one at 455 nm was below the bulk bandgap. These blue-shifted and red-shifted emission processes reveal the interplay between quantum confinement, surface states and band edge related optical transitions. We propose a model to explain the frequently observed deviation from quantum confinement in the photoluminesence trends for SiC-derived nanoparticles suspended in solvents. The quantum confined properties of the SiC structures provide a route for optical tunability in the UV-blue spectrum for use in novel photonic and biomedical applications.

I. Introduction

Silicon carbide (SiC) is known as a technologically important material for applications in harsh environments and high power applications owing to its low intrinsic carrier concentration, high chemical resistance, high thermal conductivity, and high critical electric field [1,2]. Apart from these qualities, SiC in its bulk form is an indirect bandgap material like silicon (Si) resulting in low photoluminescence (PL) quantum yield. When transformed from bulk into a porous material, visible room temperature PL is observed for porous Si (por-Si) [3-5], which in turn initiated interest in porous SiC (por-SiC) [6-12]. The enhanced blue-green PL in por-SiC has been studied for applications in light emitting devices [13-15]. The strong absorption in the ultraviolet (UV) has applications for photodetectors[16,17], while the large surface area is suitable for gas sensors [18-20]. Furthermore, as a material that is chemically inert and biocompatible, por-SiC has recently been used to produce SiC based quantum dots (QDs) for biomarkers in living cells [21-26].

As in the case of por-Si, one of the most widely used methods to produce mesoporous (2-50 nm pore size) por-SiC structures is anodic electrochemical etching of the bulk using hydrofluoric acid (HF) electrolyte [7,10]. The por-SiC can be further processed to make QDs via mechanical grinding or ultrasonication in solvents such as water, ethanol or toluene [26-29]. Typically, por-SiC in air shows sub-bandgap emission assigned to surface defects which is blue-shifted but not so much as to exceed the bulk bandgap. This is in constrast to the above bandgap PL obtained for por-Si [5,7,8,30]. However, above bandgap PL has been observed when 3C-SiC and 6H-SiC nanoparticles are suspended in solvents [27,29,31,32]. Botsoa [33] studied 6H-SiC nanopowder in ethanol where quantum confinement for the smallest nanocrystals (less

than 2 nm) was observed. It was proposed that three radiative channels are present: surface states, quantum confinement and impurity level transitions. In order to observe quantum confinement effects, surface states and impurity related mechanisms need to be suppressed.

Several experimental observations are not fully described involving 3C, 4H and 6H-SiC polytypes which unexpectedly show similar PL despite the different crystal structure and bandgaps. This has been claimed to be related to phase transformation from 4H or 6H into 3C during the ultrasonication process [34,35] based on XRD and QD lattice spacing measurements. However, the potential contributions from surface defects and surface terminations which may give rise to the similar PL characteristics remain inconclusive. There have also been reports of deviation from quantum confinement in the PL trend where emission PL peaks were constant in energy for short excitation wavelengths but red-shifted at longer excitation wavelengths. These inconsistencies are reported to be related to surface states dominating the behavior of small QDs rather than quantum confinement [36,37].

Previous research has mainly focused on 3C and 6H-SiC whilst in this work, we investigated porous 4H-SiC in ethanol prepared by the anodic electrochemical etching of bulk n-type 4H-SiC in HF/ethanol electrolyte at 20 V followed by an ultrasonication process. We provide evidence based on x-ray diffraction (XRD) and other characterisation techniques to show that the mechanism behind the PL frequently ascribed to phase transformation is likely related to band edge-impurity/defect level transitions instead of the polytypic change.

II. Experimental method

Bulk, 8º off-axis, *n*-type (10^{19} cm^{-3}) 4H-SiC wafer pieces (1 cm × 1 cm) from CREE were degreased in acetone and dipped in HF prior to silver paste being applied as the back contact. Por-SiC was prepared by anodic electrochemical etching in a teflon cell using a copper plate as the anode contact to the samples, while a tungsten wire served as the counter electrode. The electrolyte was 48 % HF/ethanol solution (1:1 by volume) [5,38]. The etching duration was one hour at an applied bias of 20 V [11] using a Keithley 2611A sourcemeter. During etching, the current flow decreased commensurate with the increase in the resistance as the porous layer was formed; the range of current was 40 mA to 10 mA and the cell resistance 0.5 kΩ to 2 kΩ respectively. The etch depths were 25-30 µm as determined from the underlying wafer pieces using a Tencor P-1 profilometer by measuring the step edge between the unetched and etched surfaces. The etching time of 1 hour at 20 V was sufficiently long to delaminate the porous layer. The resulting delaminated por-SiC (D-Por-SiC) film was removed from the wafer piece and characterised with Raman spectroscopy on a Horiba Jobin Yvon HR800UV at a wavelength of 514.5 nm in a near backscattering geometry, followed by XRD on a Bruker D8 Advance diffractometer equipped with a Cu K_α source of wavelength 1.54 Å. The D-Por-SiC film was then ultrasonicated in ethanol for 30 minutes. After sedimentation, the top portion of the solution was decanted and the resulting dispersion of sonicated porous structures in ethanol (S-Por-SiC) were characterised by high resolution transmission electron microscopy (HRTEM) on a JEOL-2100F FEG TEM operated at 200 kV and X-ray photoelectron spectoscopy (XPS) on a Thermo Theta Probe XPS spectrometer. Optical characterisation was undertaken using UV-visible absorption (UV-Vis) on a Hitachi U-3010 spectrophotometer while photoluminescence (PL) and photoluminescence excitation (PLE) were conducted on a Hitachi F-2500 fluorescence spectrophotometer. To assess the effect of the ultrasonication process in this work, D-Por-SiC (without ultrasonication) and S-Por-SiC (sonicated) samples were ground into a powder and characterised using XRD.

III. Results and discussion

A. Crystallite size

The reduction in average crystallite size supporting quantum confinement effects can be inferred from Raman scattering measurement. Figure 1 shows the D-Por-SiC delaminated from the bulk wafer after the electrochemical etch in HF/ethanol. This allows characterisation of the material without contribution from the bulk. The corresponding Raman spectrum for this layer normalised to the maximum phonon peak is compared against the bulk 4H-SiC substrate counterpart as shown in Figure 2a. In the bulk, the A_1 longitudinal optical (LO) mode at 980.3 cm^{-1} and transverse optical (TO) modes with respective E_1 and E_2 symmetries at 797.7 cm^{-1} and 777.1 cm^{-1} are observed. These correspond to known features of 4H-SiC [39-41]. The observed LO peak in this case is broad and at a higher wavenumber (980.3 cm^{-1} compared to reported 965 cm^{-1}). The blue-shift in the A_1 LO peak correspond to a high *n*-type doping concentration of about 5×10^{18} cm^{-3} [42].

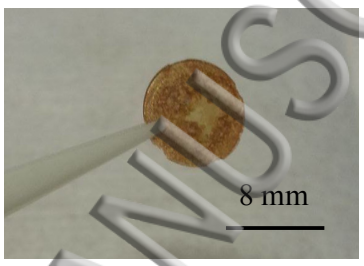

FIG. 1 D-Por-SiC prepared by anodic electrochemical etching in HF/ethanol solution.

Similarly, the D-Por-SiC Raman spectrum exhibited A_1, E_1 and E_2 phonon bands (968.1, 797.0, 776.5 cm^{-1}) indicating that 4H polytype crystallinity was preserved after the etch process. Peaks near 785 cm^{-1} for both bulk and D-Por-SiC are ascribed to the formally Raman forbidden A_1 (TO)[43] peak allowed in this case likely due to the off-axis orientation[44] or crystal imperfection. Breaking of the crystal lattice periodicity and selection rules for D-Por-SiC

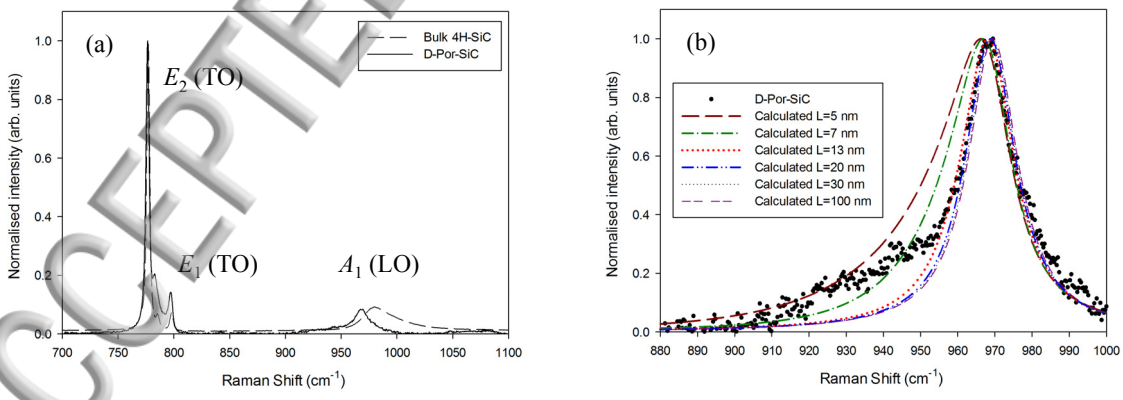

FIG. 2 (a) Raman spectra of bulk 4H-SiC and D-Por-SiC, (b) A_1 LO mode line shape analysis based on phonon confinement model.

resulted in enhanced TO peaks' intensities compared to the bulk. There are red-shifts in frequencies in the TO and LO peaks for D-Por-SiC compared to the bulk. The red-shifts in the

This manuscript was accepted by J. Appl. Phys. Click here to see the version of record.

TO peaks are less than 1 cm^{-1}, from 797.7 cm^{-1} to 797.0 cm^{-1} (Figure 2(a)) and 777.1 cm^{-1} to 776.5 cm^{-1} for E_1 and E_2 respectively at the measurement spectral resolution of 0.3 cm^{-1}. The A_1 (TO) peak was red-shifted by 3 cm^{-1} from 785.7 cm^{-1} to 782.7 cm^{-1}.The LO peak red-shifted significantly by approximately 12.2 cm^{-1} from 980.3 cm^{-1} to 968.1 cm^{-1}.

The observed 12.2 cm^{-1} red-shift and a narrower D-Por-SiC LO mode peak frequency may be the combined effects of quantum confinement of optical phonons [45] and free carrier depletion as a result of surface trapping[46]. If the latter is true then based on the red-shift, the free carrier concentration has decreased from around 5×10^{18} cm^{-3} to 3×10^{18} cm^{-3} [42]. In addition, the LO mode peak is accompanied by an asymmetric broadening to the low frequency side (Figure 2(b)). In relation to quantum confinement, the Raman line shapes can be quantitatively described by the phonon confinement model (PCM) [7,45], given by

$$I(\omega)\propto\int_0^1\frac{e^{-q^2L^2/4c^2}}{[\omega-\omega(q)]^2+\frac{\tau_o^2}{2}}d^3q \qquad (1)$$

where $I(\omega)$ is the Raman scattering intensity, ω is the Raman frequency, q is the reduced wave vector ($q=q'/q'_{max}$), where q' is in units of the reciprocal lattice vector $2\pi/c$ and $q'_{max}=4\pi/c$ [40] for 4H-SiC, lattice parameter along the c-axis, c=1.0053 nm[47], τ_o is the line width in the bulk crystal, L the diameter of the nanocrystal and $\omega(q)$ is the phonon dispersion relation for A_1 LO mode approximated by

$$\omega^2(q)=A+B\cos\left(\frac{\pi q}{2}\right) \qquad (2)$$

where the values $A=702\times10^3$ cm^{-2} and $B=238\times10^3$ cm^{-2} are adapted from 4H-SiC phonon dispersion given by Feldman *et al.* [40]. PCM is not commonly applied to the acoustic modes due to their energy being zero at the Brillouin zone center and is rarely used for TO modes because of their low phonon dispersion. It is almost exclusively applied to the LO modes[48]. To simplify the calculations, the Brillouin zone is assumed to be spherical and the dispersion curve isotropic; these assumptions are justified as only a small region centered at Γ in the Brillouin zone contributes to the scattering[49]. According to the PCM model [7,49], an asymmetric broadening and a red-shift in the LO peak is expected for nanostructures whose finite sizes result in relaxation of the selection rule for Raman scattering, allowing transitions with $\Delta q\neq0$. The average crystallite size for which equation (1) was used in Ref. [7] was 25 nm which is comparable to our ~20 nm size scales as will be shown later in the text. The 12.2 cm^{-1} red-shift in frequency in the A_1 LO peak for the D-Por-SiC compared to that of the bulk in Figure 2(a) is relatively large in comparison to Ref. [7] where red-shifting of the LO peak was not observed. Considering the average crystallite size of ~20 nm, it is possible that most of the observed red-shift of the A_1 LO mode from the peak position of the bulk may be related to free carrier depletion due to surface states in the porous material in contrast to our starting bulk material that was highly doped. Being heavily doped, the bulk material showed a blue-shifted LO mode associated with phonon coupling with free carrier plasma of electrons (LO phonon-plasmon coupling).

In terms of line shape, Figure 2(b) compares the experimental A_1 LO mode for D-Por-SiC to the calculated phonon confined line shapes for different crystallite sizes based on the PCM model. The experimental LO peak is asymmetric and exhibits a shoulder at the low frequency side consistent with relaxation of selection rules allowing contributions from the negative dispersion of the optical phonon branch away from the zone center. A comparison of the

calculated line shapes with the experimental data indicates that the average crystallite diameter in the D-Por-SiC sample is approximately 13 nm. It should be noted that other factors such as surface modes of small particles smaller than the excitation wavelength (Fröhlich modes) [7] unique to porous polar semiconductors can contribute to the Raman line shape at the low frequency side. Like the LO phonon mode, the Fröhlich mode can also couple with the plasmon mode that may further influence the position of the peak frequency. Therefore we have also analysed the particle size using XRD and electron microscopy. Both the observed asymmetric broadening at the low frequency side and red-shifting are strong indications of the existence of nanocrystallites small enough for phonon confinement to occur in the D-Por-SiC, whilst its slight deviation from the theoretical line shape (920-950 cm^{-1} region) may be influenced by surface phonons [7]. Previous investigations for por-SiC have reported mixed results in that LO broadening was observed but the peaks had negligible shift or showed a blue-shift instead of a red-shift due to surface phonon-plasmon coupling [7,13,50-52]. These could be the combined effects of diffuse scattering, spectral line broadening and violation of symmetry selection rules [7].

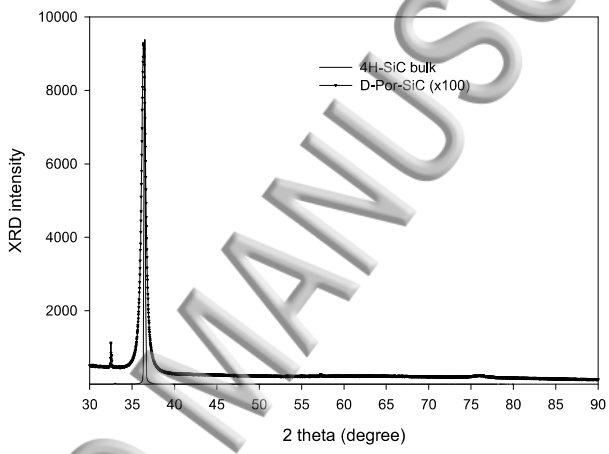

FIG. 3 XRD pattern for bulk 4H-SiC and D-Por-SiC.

Figure 3 shows the XRD patterns for bulk 4H-SiC and D-Por-SiC (magnified by a factor of 100). Both show sharp peaks near the 2θ Bragg angle of 36º associated with the (0004) SiC planes. A peak near 33º for D-Por-SiC associated with the $(10\bar{1}0)$ SiC plane is visible in the D-Por-SiC data indicating disorder was introduced as new porous structures associated with this plane were formed during the etching process. These peaks show that the D-Por-SiC was highly crystalline and parts of the remaining etched skeletal structure retained the long range order of the bulk. However, there is a broadening in the XRD peak for D-Por-SiC compared to the bulk, and the full width at half of maximum (FWHM) is 0.6º. The peak broadening suggests a reduction of the average crystallite size in D-Por-SiC. The calculated average crystallite diameter by Scherrer's method [53] is about 13 nm for the D-Por-SiC being in close agreement with the average diameter calculated from the Raman spectrum.

The D-Por-SiC layer was broken up by sonication in ethanol producing dispersed S-Por-SiC particles. Figure 4(a) shows the HRTEM image of S-Por-SiC structure dried off from ethanol solution. The S-Por-SiC represented a skeleton of the original bulk 4H-SiC with mesopores spread throughout the structure. The interpore spacings consist of interconnecting thin walls. Figure 4(b) is the zoomed in image showing representative dimensions within the S-Por-SiC structure where the average interpore spacing (A) is 16.9±5.5 nm, smallest wall dimension (B) of 2.9±1.0 nm, pore diameter (C) of 30.5±6.3 nm and depth (D) of

This manuscript was accepted by J. Appl. Phys. Click here to see the version of record.

approximately 25 nm. We note that the value of the depth (D) is approximate as it may be distorted by the perspective of the image. The areal porosity of the structure is determined to be 0.37 by means of image analysis using ImageJ.

The size estimates inferred from the Raman and XRD of approximately 13 nm appear to corroborate with the interpore spacing (A) of 17 nm. It is noted that for Raman scattering in a perfect backscattering configuration, the TO mode peaks (planar mode) arise from atomic vibrations perpendicular to the c-axis while the LO mode peak (axial mode) originates from vibrations that are parallel to the c-axis. Figure 4(c) shows that the atomic planes within the interpore spacings have an average interplanar spacing of 0.267 nm corresponding to the distance between 4H-SiC $(10\bar{1}0)$ planes. This suggests that the dimensions in the plane of the image are nearly perpendicular to the c-axis. Therefore the small interpore dimensions (A and B) relate to the TO modes while the LO mode relates to the larger dimensions of depth into the pore (D).

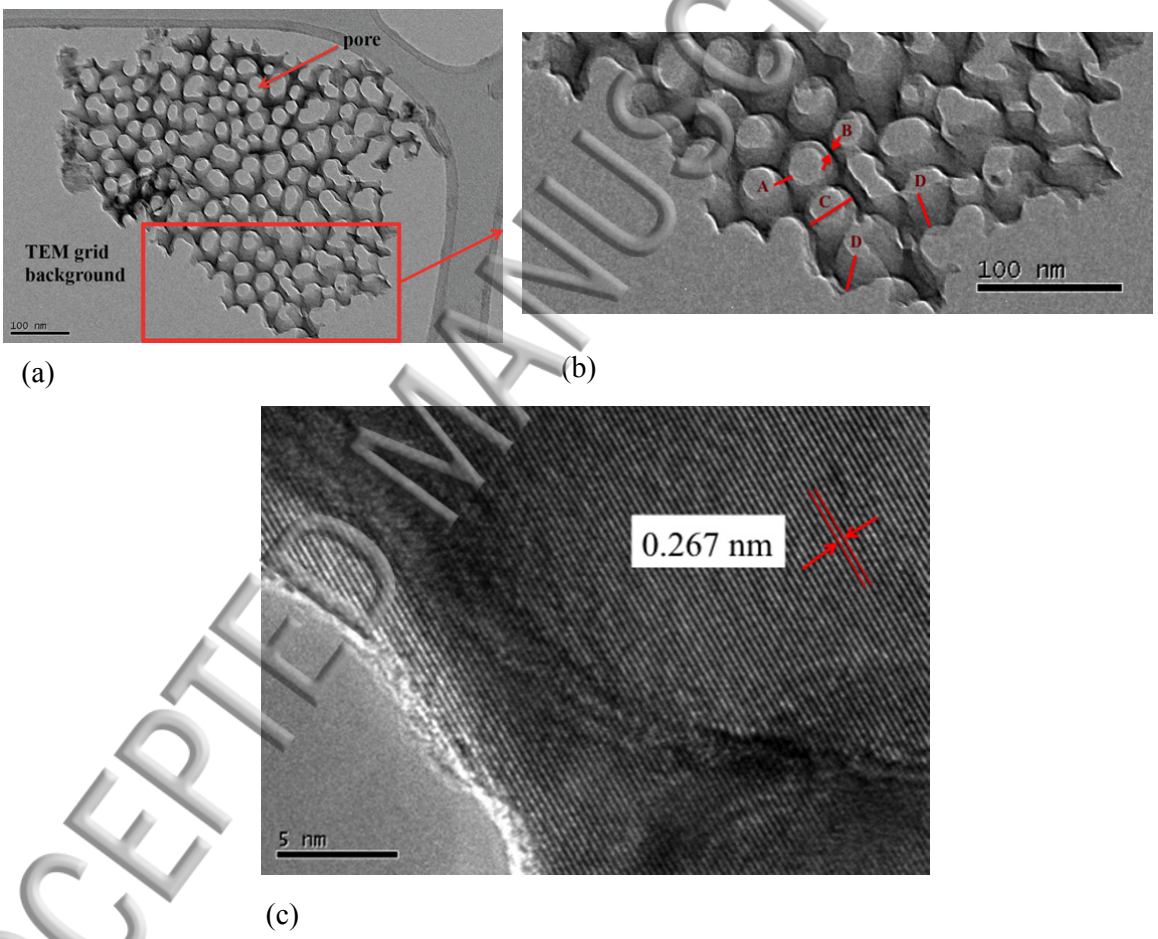

FIG. 4 HRTEM images of (a) mesoporous S-Por-SiC particle consisting of a network of interconnected thin walls, (b) zoomed in image of S-Por-SiC showing the labelled dimensions of thin walls and pore diameter with average sizes as stated in the text, and (c) the average interplanar spacing of 0.267 nm corresponding to 4H-SiC $(10\bar{1}0)$ planes.

A plausible explanation as to why the LO mode may red-shift in the case of larger dimensions is the shape effect, stemming from the long-range dipolar interactions as reported for polar

semiconductor nanowires[54]. It has been observed that polar semiconductor nanowires with lengths of several microns and diameters of ~20 nm exhibited red-shift and asymmetric broadening in the LO mode and the effect strengthened with larger aspect ratio. The prominent shift in the LO mode can be attributed to its larger phonon dispersion width in comparison to other Raman lines.

In our study, the XRD provides a better estimation of the interpore spacing. The XRD data also suggest that the sonication process did not result in a phase change in the 4H polytype as has been reported for 4H and 6H-SiC based QDs after ultrasonication where interplanar spacings of 0.217 nm for 3C $(20\bar{2}0)$ planes [34] and 0.195 nm for 3C $(21\bar{3}0)$ planes [35] were found.

The inferred average crystallite size of 13 nm from XRD for the por-SiC structure is consistent with the average size of 17 nm observed in HRTEM. The nanoscale lengths of around 2 nm at the wall's edges may potentially support quantum size effects where spatial localisation of photogenerated carriers in the mesoporous 4H-SiC structure can increase the emission intensity and energy.

B. Chemical composition

As not only quantum size effects govern the optical properties of nanostructures, the chemical composition, particularly at the surface needs to be investigated. XPS with probing depths of up to 10 nm of the surface is suitable for this purpose. The high resolution core level XPS spectra for S-Por-SiC drop-casted on gold foils are shown in Figure 5 plotted as counts per second versus binding energy.

The high resolution XPS spectrum of Si 2*p* for S-Por-SiC in Figure 5(a) shows a peak at 100.64 eV indicating the existence of SiC bonds [55-57] in the porous structure. In addition, other chemical states for Si 2*p* in S-Por-SiC involve silicon oxycarbide (102.10 eV) [58] and SiO_2 (103.70 eV)[59], which indicate oxidation of Si as a result of the anodic etch process. As the HF solution dissolves SiO_2 during etching, it is likely that the exposed Si with dangling bonds oxidized in air after the process. We attribute the peak at 105.40 eV to SiF_x bonds in the S-Por-SiC [60,61] which relates to the chemical interaction with HF.

Figure 5(b) shows that C 1*s* for S-Por-SiC consists of Si-C bonds (282.65 eV) and surface reconstructions of C sp^3 dimers (284.30 eV) and C-O bonds (286.05 eV)[58]. Surface terminations as a result of chemical interaction with ethanol and HF may have resulted in C bonding in carbonyl (C=O) or carboxyl groups (COOH) (288.20 eV) [62,63] and C-F (290.10 eV) [64]. S-Por-SiC O 1*s* peaks in Figure 5(c) show SiO_2 and C-O bonds [58] which may have arisen from the interaction with water or ethanol. In the literature[10] the following electrochemical reactions have been proposed for the electrochemical etching of SiC in HF/ethanol electrolyte:

$$SiC+2H_2O+4h^+ \rightarrow SiO+CO+4H^+$$

$$SiC+4H_2O+8h^+ \rightarrow SiO_2+CO_2+8H^+.$$

The dissolution of SiC commences only when anodic currents are present whereby holes are required to be supplied at the SiC-electrolyte interface. By applying a large enough positive (reverse bias) to *n*-type SiC, no photoassistance is required as in our case to etch SiC. Water is directly involved in the etching process producing Si-O and C-O based by-products. Ethanol is added to electrolytes for the formation of porous semiconductors to reduce the surface

tension at the solid/electrolyte interface and allow the aqueous electrolyte to penetrate the pores[65]. Viscosity is a secondary factor. HF serves to remove the oxide. However, as F has been traced to form bonds with Si and C in the XPS spectra, ethanol might also terminate on unsatisfied dangling bonds of the porous material.

Thus, the core level Si 2*p*, C 1*s* and O 1*s* spectra indicate that SiF_x, SiO_2, C-C, C=O/COOH, C-F and C-O bonds on the S-Por-SiC surface resulted from the etching process in HF/ethanol electrolyte and subsequent dispersion in ethanol[66]. These bonds are potentially the make up of surface terminations (such as fluorine) and surface defects (C=O/COOH) that would introduce surface states influencing the optical properties of S-Por-SiC. Exposure to air in addition to the etching process and subsequent dispersion in ethanol might play a role in the formation of some of the surface groups, since the material must be dried before some of the characterization techniques can be applied.

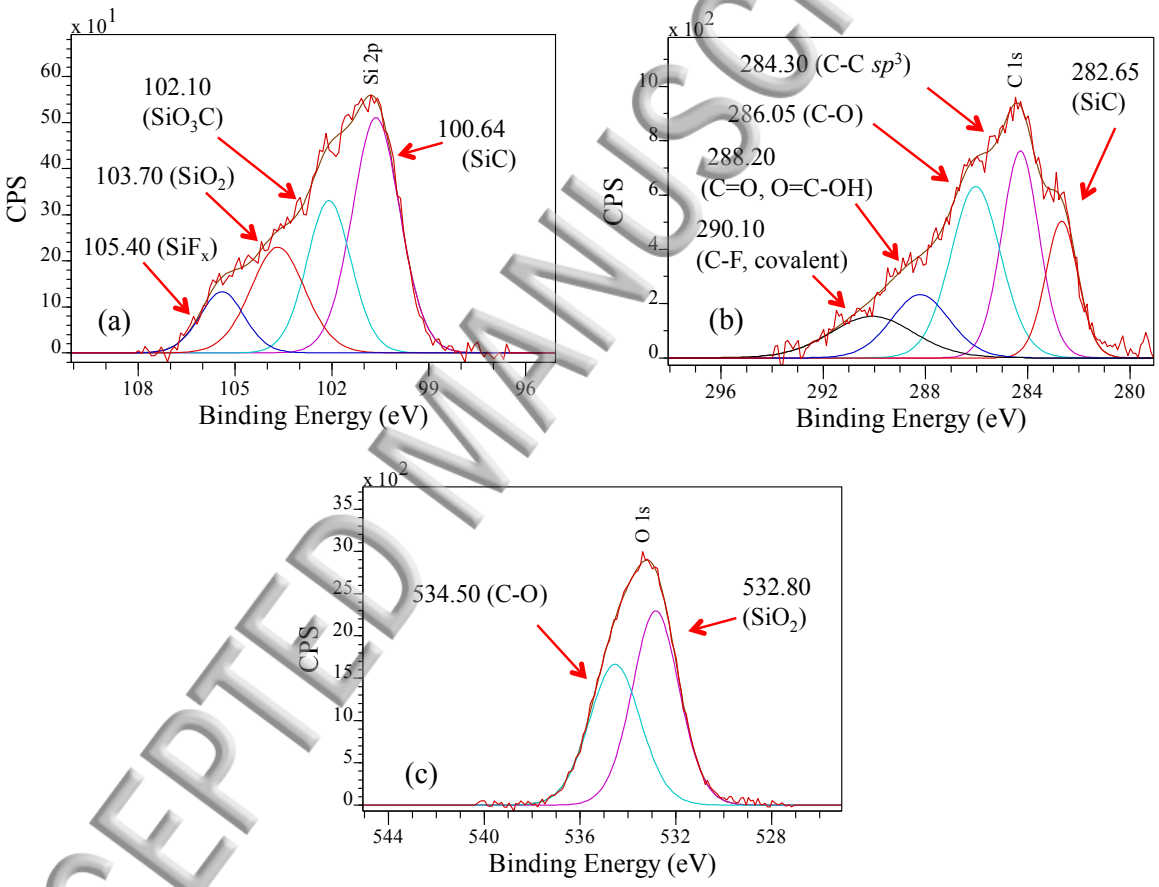

FIG. 5 Core level Si 2*p*, C 1*s* and O 1*s* XPS spectra for S-Por-SiC (a), (b), (c) respectively.

C. Optical characterisation

We assess the effects of nanostructuring and surface terminations/defects upon the S-Por-SiC's optical properties via UV-Vis absorption, PL and PLE measurements. Figure 6 shows UV-Vis absorbance spectra in ethanol dispersion. Pure ethanol without S-Por-SiC showed very little absorbance in comparison to the S-Por-SiC dispersion. The 4H-SiC substrate showed a prominent below bulk bandgap absorption peak at 462.9 nm or 2.67 eV (Figure

6(a)) which was widely reported in the literature in terms of *n*-type N donor [67-69] assisting interconduction band transitions at the M point. We are suggesting the Z_1 center[70] located at E_C-0.63 eV where its energy approximately matches ~2.6 eV as a possible contributor. The fundamental absorption occurred near 383 nm or 3.23 eV (dotted vertical line) consistent with the indirect energy gap for bulk 4H-SiC [71].

The absorption spectrum for S-Por-SiC incorporates multiple scattering of which Rayleigh scattering is predominant and does not show the free carriers or defect related peak. Below 380 nm, the absorption increases as smaller particles were being excited. An onset in absorption occurred around 290 nm (4.27 eV). As the shoulder was broad, the absorption would be better resolved and further verified by PLE which will be discussed later in the text. The increased absorption for wavelengths shorter than 290 nm may be contributed by the mesoporous structures with nanometric scale walls that have energy gaps larger than the bulk. The energy gaps at the M, L and Γ points of the Brillouin zone for bulk 4H-SiC are 3.23 eV,~4.00 eV and 5-6 eV respectively[72,73]. The energy at the onset of 290 nm (4.27 eV) for S-Por-SiC is larger than the energy gap of bulk 4H-SiC at the M and L points indicating that lowering of the lattice symmetry by size effects may have increased the indirect energy gap [74].

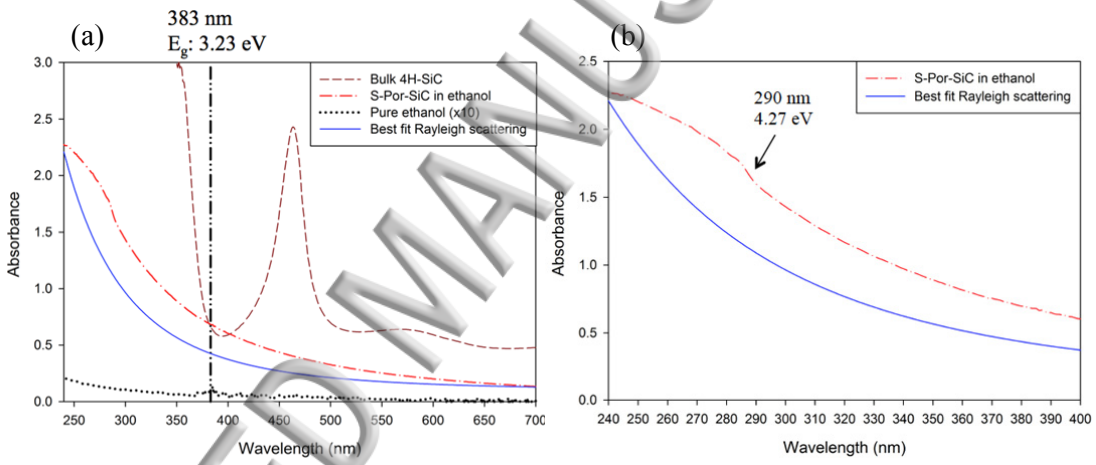

FIG. 6 (a) UV-Vis absorption spectra of bulk 4H-SiC, S-Por-SiC and pure ethanol, (b) zoomed in absorption spectrum of S-Por-SiC showing absorption onset near 290 nm region.

In verifying quantum confinement, the shift in PL peak position with respect to the change in excitation wavelength can be used. One explanation is that as the excitation energy is decreased (longer wavelengths) only larger QDs are excited and therefore the PL energy is expected to decrease (red-shift towards longer wavelengths). The red-shifting in PL peaks with increasing excitation wavelengths is another means of confirming the existence of the quantum size effects[27,31,35,75,76].

Figure 7(a) shows the PL spectra at room temperature for bulk 4H-SiC and S-Por-SiC in ethanol for a range of excitation wavelengths. S-Por-SiC exhibited enhanced PL emission with an intensity approximately 100 times greater than the bulk.

For excitations in the range 250-279 nm, above bulk bandgap PL emission peaks and shoulders (above 4H-SiC E_g: 3.23 eV, 383 nm) that were relatively constant with excitation wavelength were produced, with the primary peaks obtained near (i) 303 nm and secondary shoulders near (ii) 345 nm. The typical FWHM values were 50 nm. Whilst the two orders of magnitude increase in intensity and above bandgap PL features (303 nm and 345 nm) are

indications of quantum confinement within the thin walls of S-Por-SiC, the expected red-shifting with changing excitation energies was not observed.

For excitation wavelengths in the range 320-400 nm, PL features were mainly below the bulk bandgap and red-shifting from 455 to 470 nm (iii) whilst a contribution from above gap was possibly associated with the 345 nm feature. These peaks were broader with typical FWHM values of around 150 nm.

The excitation wavelength-independent PL peaks at short excitation wavelengths and red-shifting PL peaks at longer wavelengths are counterintuitive to quantum confinement theory and have been reported previously for SiC QDs in solvents [34,66]. In general, previous reports have ascribed excitation wavelength-independent PL peaks around 450 nm to SiC-QDs dominated by surface states (diameters smaller than 3-4 nm) whilst the red-shifting PL peaks were due to quantum confinement in the larger QDs (larger than 3 nm) that were not affected by surface states [34,77].

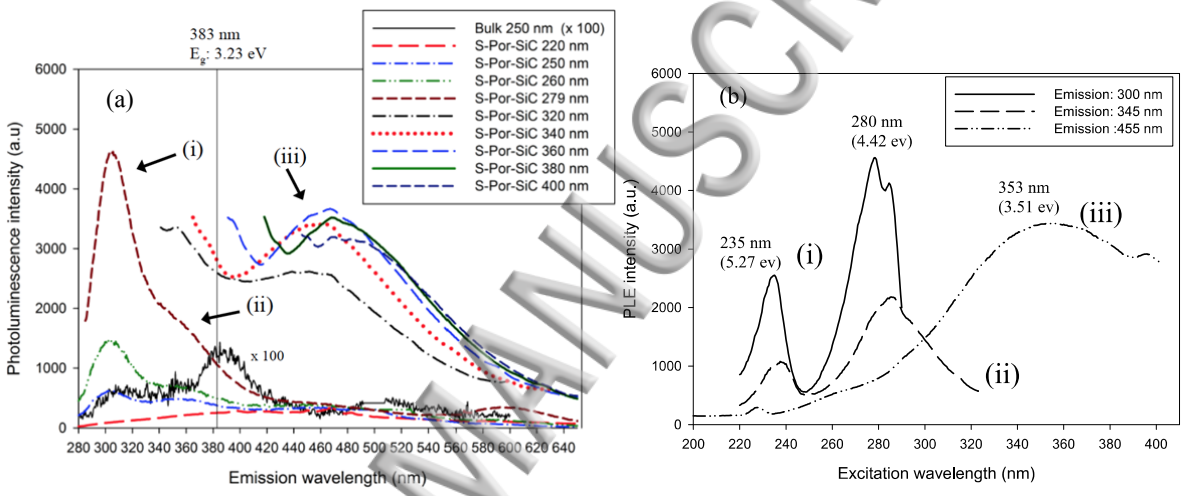

FIG. 7 (a) PL emission spectra of bulk 4H-SiC and S-Por-SiC suspended in ethanol at different excitation wavelengths. Numerals (i), (ii) and (iii) indicate main designated PL emission peaks at 300 nm, 345 nm and 455 nm. (b) PLE spectra under different monitoring wavelengths for designated PL peaks to probe the absorption transitions preceding emission.

In order to distinguish the origins of the constant above bandgap and the red-shifting below bandgap PL peaks, the absorption processes preceding radiative recombination were probed by photoluminescence excitation spectroscopy (PLE) [4].

Figure 7(b) shows the PLE spectra monitored at the PL emission wavelengths of interest; (i) 300 nm, (ii) 345 nm and (iii) 455 nm. The above bulk bandgap, excitation wavelength-independent PL emission peaks at (i) 300 nm and (ii) 345 nm in Figure 7(a) were preceded by absorptions at similar energies near (i) 235 nm (5.27 eV) and (ii) 280 nm (4.42 eV) as shown in Figure 7(b). The PLE peak at 280 nm correlates with the absorption feature observed via UV-Vis spectroscopy in Figure 6(b). These PLE peaks were narrow, suggesting transitions between discrete states and high above the bulk bandgap. The PLE peak at 235 nm (5.27 eV) is rarely reported and may be related to the direct optical transition at the Γ point of 4H-SiC[73].

On the other hand, the rather broad, below bulk bandgap and red-shifting PL emission peaks (iii) from 455 nm towards ~470 nm as shown in Figure 7(a) originated from a broad absorption band with a PLE peak near the band edge at (iii) 353 nm (Figure 7(b)).

Since the red-shifting PL peaks in this work were very broad and below the bulk bandgap at around 455 nm, we ascribe them to surface defects or possibly donor impurities as has been reported for 6H-SiC porous SiC [8].

It is noted that 4H-SiC QDs were shown to have sub-bandgap PL peaks around 450 nm with corresponding PLE peaks at 297 nm, 323 nm and 365 nm [34]. The sub-bandgap PL peak around 450 nm for 4H-SiC was ascribed to hexagonal to cubic phase transformation during ultrasonication resulting in similar PL emission and a common PLE peak near 365 nm for all polytypes. Thus, we next assess the effect of ultrasonication by XRD on the sonicated versus unsonicated por-SiC.

D. Effect of ultrasonication

We assessed the effect of our ultrasonication process on the 4H-SiC polytype by XRD on ultrasonicated, dried and mechanically ground S-Por-SiC and mechanically ground D-Por-SiC (without ultrasonication) as shown in Figure 8. In powdered form, a higher number of XRD peaks relating to the randomised crystallites appeared. These peaks were consistent with 4H polytype for both sonicated S-Por-SiC and unsonicated D-Por-SiC. This is in agreement with S-Por-SiC's interplanar spacing of 0.267 nm relating to 4H-SiC $(10\bar{1}0)$ via HRTEM. Thus the below bulk bandgap and red-shifting PL peaks in this work were not related to polytype transformation from 4H-SiC into 3C-SiC, but were likely a result of 4H-SiC band edge transitions with surface defects or donor impurities found in the larger sized crystallites. Band edge, above bandgap related PL has been observed previously [36] and associated with larger size 3C-SiC QDs (5-30 nm). The reported excitation wavelength-independent PL emission at 450 nm assigned to surface states and near band edge PLE peak at 365 nm that are common for 3C, 6H and 4H-SiC QDs [34] suggest that both quantum confinement and surface states/defects dictate the optical properties of SiC nanostructures as we explain in section IV.

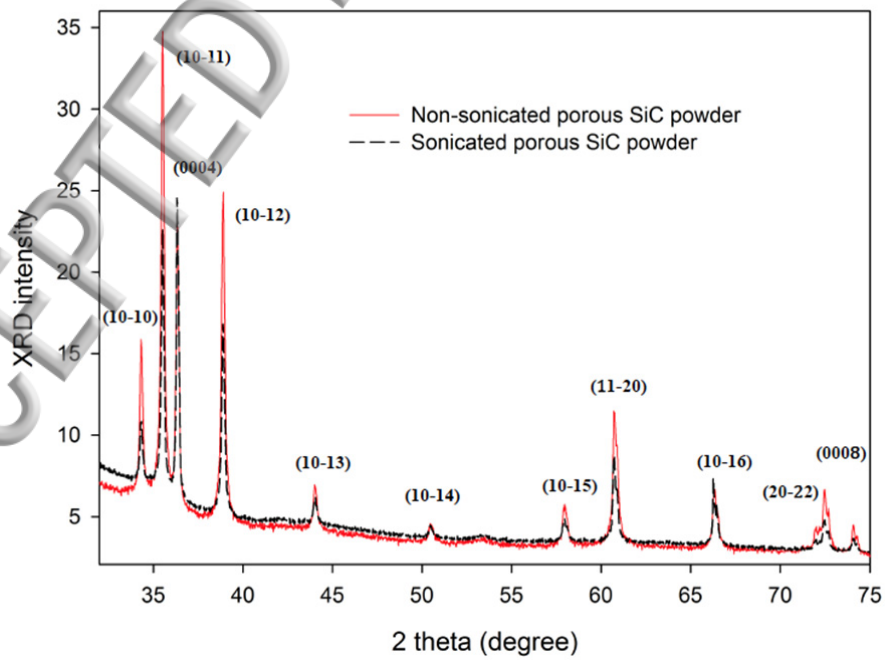

FIG. 8 XRD pattern comparing ground S-Por-SiC and D-Por-SiC samples.

IV. Model for quantum confinement and surface states dependent emission

We present the model described using Figure 9 which illustrates the observed emission processes. We refer to the top most valence energy level and bottom most conduction energy level associated with Si and C atoms within the crystallite as core HOMO (highest occupied molecular orbital) and core LUMO (lowest unoccupied molecular orbital) respectively, while those related to surface atoms are referred to as surface HOMO and surface LUMO respectively. As the crystallite size decreases, the core HOMO-LUMO gap, related to the Si and C atoms in the interior of the crystallite (core atoms) widens due to quantum confinement. At sufficiently small sizes, the HOMO-LUMO energy difference is large enough for surface states (surface HOMO and LUMO related to atoms at the crystallite's surface) to dominate the optical gap causing the excitation wavelength-independent PL emissions in region A. These surface states may obscure the underlying quantum confinement as density functional theory (DFT) calculations and experiments have shown that surface groups such as carboxyl (-COOH), C-O, and fluorine (-F) may introduce fixed energy levels (surface atoms' HOMO and LUMO) within the energy gap of SiC nanoparticles [78-81] rendering the optical properties size independent. As the core-related HOMO and LUMO (relating to the interior of the crystallite) narrow with increasing size, the surface states lose their influence allowing transitions between core HOMO and core LUMO to dominate causing red-shifting of the above bandgap emission PL in region B, exhibiting size dependent optical properties. As the crystallites' sizes increase further, donor impurities become important [33] as more dopants are available in larger crystallites and on average more defects may be found within a larger crystallite. The optical transitions now constitute the core HOMO with donor impurity/defect states near the core LUMO producing below bandgap and red-shifting PL emissions in region C. As the crystallite size approaches bulk-like dimensions in region D, the HOMO and LUMO represents the respective bulk valence band and conduction band edges. For the bulk, excitation wavelength-independent and below bulk bandgap PL dominates, as shown by region D. In this work, due to surface states introduced by fluorine surface termination, we observe excitation wavelength-independent PL emissions in region A, while oxygen related defects in C=O/COOH bonds and N doping are ascribed to the red-shifting below bulk bandgap PL emissions in region C [33,82]. The PL peak then becomes independent of size with a peak wavelength of ~470 nm in region D. It is difficult to assign the precise transition involved, but the energy approximately matches that of the absorption peak in Figure 6(a) or the energy of the Z_1 center[70].

The model presented here is in conceptual agreement with the theoretical model given by Wolkin *et al.* for Si QDs in porous Si (pristine versus oxidised porous Si)[83] and our DFT calculations on 4H-SiC quantum dots (–H versus –F and –OH surface terminations)[84], where both quantum confinement and surface passivation determine the electronic states of the QDs.

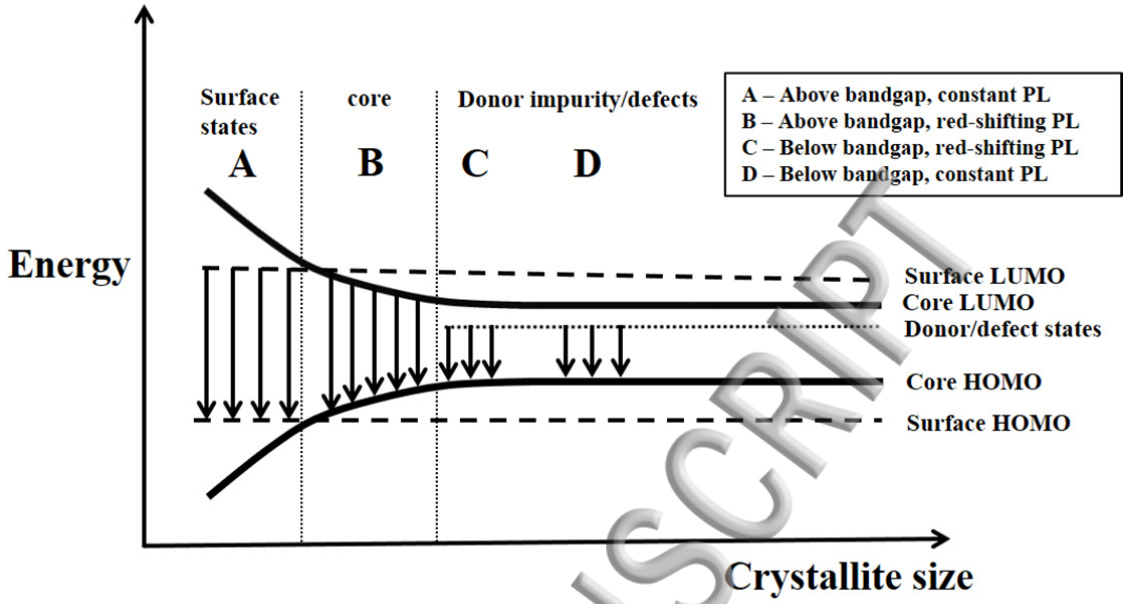

FIG. 9 Illustration of the interplay between quantum confinement and surface states for small crystallites and donor impurities/defects for larger crystallites on the optical transitions of por-SiC.

V. Conclusions

To conclude, the 4H polytype por-SiC in ethanol exhibited three PL bands: two of which were above bandgap, narrow, quantum confined and surface states related, and in the UV (300 and 345 nm); whereas the third PL band was below bandgap, broad, donor impurity/defect related, and in the visible spectral range (455 nm). These UV and visible range emission bands are accessible by high and low excitation energies respectively (excitation wavelengths of 235 and 280 nm for the former and 353 nm for the latter). In addition to quantum confinement of the por-SiC, surface states formed by fluorine surface termination groups as a result of etching in HF electrolyte and subsequent suspension in ethanol are ascribed to the excitation wavelength-independent emission in the UV. Donor impurity, C=O/COOH surface groups, defects and diminishing quantum confinement in larger sized crystallites are assigned to the band edge transitions that are responsible for the broad sub-bandgap emission. Engineered surface terminations such as fluorine along with defect control and intentional impurity doping, may be used to control electronic states in novel optoelectronic devices or biomedical applications. The por-SiC is a promising material in producing nanocrystals having absorption and emission in the UV that may be applicable for UV photodetectors and wavelength downconvertors whereas emission in the visible range may find applications for non-toxic biomarkers.

In summary, we have fabricated por-SiC from *n*-type 4H-SiC substrates via anodic electrochemical etching in HF/ethanol solution followed by an ultrasonication process. The average crystallite size, porous structure, crystallinity and polytype have been verified by Raman scattering, HRTEM, and XRD. Via UV-Visible absorption, PL and PLE, we revealed above and below bulk bandgap absorption/emission processes related to the interplay between quantum confinement, surface states and donor impurity/defects related optical transitions.

Though common PL characteristics across different SiC polytypes of dissimilar band gaps have been widely reported, an explanation to account for this observation remains elusive. We propose a model to explain the observed constant and red-shifting of the PL emissions seen in SiC based nanoparticles in solvents. Finally, we note therefore that it is critical to understand the chemical and physical features of SiC derived nanostructures surfaces as control of surface states is a requisite to exploiting the size-dependent optical properties.

Acknowledgements

We would like to thank the Ministry of Higher Education Malaysia and Universiti Sains Malaysia for the postgraduate student sponsorship.

Reference

1 A. Horsfall and N. Wright, Phys World **19,** 34 (2006).
2 N. G. Wright and A. B. Horsfall, J. Phys. D: Appl. Phys. **40,** 6345 (2007).
3 L. T. Canham, Appl. Phys. Lett. **57,** 1046 (1990).
4 A. G. Cullis, L. T. Canham, and P. D. J. Calcott, J. Appl. Phys. **82,** 909 (1997).
5 B. R. Horrocks, in *Handbook of Porous Silicon* (Springer, 2014), p. 671.
6 V. P. Parkhutik, F. Namavar, and E. Andrade, Thin Solid Films **297,** 229 (1997).
7 T. L. Rittenhouse, P. W. Bohn, T. K. Hossain, I. Adesida, J. Lindesay, and A. Marcus, J. Appl. Phys. **95,** 490 (2004).
8 O. Jessensky, F. Müller, and U. Gösele, Thin Solid Films **297,** 224 (1997).
9 G. Gautier, J. Biscarrat, T. Defforge, A. Fèvre, D. Valente, A. Gary, and S. Menard, J. Appl. Phys. **116,** 223705 (2014).
10 Y. Shishkin, W. J. Choyke, and R. P. Devaty, J. Appl. Phys. **96,** 2311 (2004).
11 Y. Ke, Y. Shishkin, R. P. Devaty, and W. J. Choyke, in *Porous Silicon Carbide and Gallium Nitride: Epitaxy, Catalysis, and Biotechnology Applications*, edited by R. M. Feenstra, Wood, C.E.C (John Wiley & Sons, Ltd, 2008), p. 1.
12 T. Cao, Y. Cheng, H. Zhang, B. Yan, and Y. Cheng, Journal of Materials Chemistry C **3,** 4876 (2015).
13 T. Matsumoto, J. Takahashi, T. Tamaki, T. Futagi, H. Mimura, and Y. Kanemitsu, Appl. Phys. Lett. **64,** 226 (1994).
14 H. Mimura, T. Matsumoto, and Y. Kanemitsu, Appl. Phys. Lett. **65,** 3350 (1994).
15 H. Mimura, T. Matsumoto, and Y. Kanemitsu, Solid-State Electronics **40,** 501 (1996).
16 N. Naderi and M. R. Hashim, Mater. Res. Bull. **48,** 2406 (2013).
17 N. Naderi and M. R. Hashim, J. Alloys Compd. **552,** 356 (2013).
18 E. J. Connolly, B. Timmer, H. T. M. Pham, J. Groeneweg, P. M. Sarro, W. Olthuis, and P. J. French, Sensors and Actuators B: Chemical **109,** 44 (2005).
19 K.-S. Kim and G.-S. Chung, Sensors and Actuators B: Chemical **157,** 482 (2011).
20 K. S. Kim, G. S. Chung, A. A. Al-Ghamdi, and F. Yakuphanoglu, Microsystem Technologies **19,** 1221 (2013).
21 D. Beke, Z. Szekrényes, D. Pálfi, G. Róna, I. Balogh, P. A. Maák, G. Katona, Z. Czigány, K. Kamarás, and B. Rózsa, J. Mater. Res. **28,** 205 (2013).
22 J. Fan and P. K. Chu, Small **6,** 2080 (2010).
23 B. Somogyi and A. Gali, J. Phys.: Condens. Matter **26,** 143202 (2014).
24 J. Fan, H. Li, J. Jiang, L. K. Y. So, Y. W. Lam, and P. K. Chu, Small **4,** 1058 (2008).

25 B. Somogyi, V. Zolyomi, and A. Gali, Nanoscale **4,** 7720 (2012).
26 J. Botsoa, V. Lysenko, A. Géloën, O. Marty, J. M. Bluet, and G. Guillot, Appl. Phys. Lett. **92,** 173902 (2008).
27 J. Y. Fan, X. L. Wu, H. X. Li, H. W. Liu, G. G. Siu, and P. K. Chu, Appl. Phys. Lett. **88,** 041909 (2006).
28 D. Beke, Z. Szekrényes, I. Balogh, Z. Czigány, K. Kamarás, and A. Gali, J. Mater. Res. **28,** 44 (2013).
29 A. M. Rossi, T. E. Murphy, and V. Reipa, Appl. Phys. Lett. **92,** 253112 (2008).
30 A. O. Konstantinov, A. Henry, C. I. Harris, and E. Janzén, Appl. Phys. Lett. **66,** 2250 (1995).
31 X. L. Wu, J. Y. Fan, T. Qiu, X. Yang, G. G. Siu, and P. K. Chu, Phys. Rev. Lett. **94,** 026102 (2005).
32 Y. Zakharko, J. Botsoa, S. Alekseev, V. Lysenko, J. M. Bluet, O. Marty, V. A. Skryshevsky, and G. Guillot, J. Appl. Phys. **107,** 013503 (2010).
33 J. Botsoa, J. M. Bluet, V. Lysenko, L. Sfaxi, Y. Zakharko, O. Marty, and G. Guillot, Physical Review B **80,** 155317 (2009).
34 J. Fan, H. Li, J. Wang, and M. Xiao, Appl. Phys. Lett. **101,** 131906 (2012).
35 X. Guo, D. Dai, B. Fan, and J. Fan, Appl. Phys. Lett. **105,** 193110 (2014).
36 D. Beke, Z. Szekrenyes, Z. Czigany, K. Kamaras, and A. Gali, Nanoscale **7,** 10982 (2015).
37 J. Zhu, S. Hu, W.-W. Xia, T.-H. Li, L. Fan, and H.-T. Chen, Mater. Lett. **132,** 210 (2014).
38 L. H. Lie, M. Duerdin, E. M. Tuite, A. Houlton, and B. R. Horrocks, J. Electroanal. Chem. **538,** 183 (2002).
39 S. I. Nakashima and H. Harima, Physica Status Solidi (A) **162,** 39 (1997).
40 D. W. Feldman, J. H. Parker, W. J. Choyke, and L. Patrick, Physical Review **173,** 787 (1968).
41 M. Chafai, A. Jaouhari, A. Torres, R. Antón, E. Martín, J. Jiménez, and W. C. Mitchel, J. Appl. Phys. **90,** 5211 (2001).
42 J. C. Burton, L. Sun, M. Pophristic, S. J. Lukacs, F. H. Long, Z. C. Feng, and I. T. Ferguson, J. Appl. Phys. **84,** 6268 (1998).
43 S. Nakashima, T. Mitani, J. Senzaki, H. Okumura, and T. Yamamoto, J. Appl. Phys. **97,** 123507 (2005).
44 H. Harima, S. I. Nakashima, and T. Uemura, J. Appl. Phys. **78,** 1996 (1995).
45 H. Richter, Z. P. Wang, and L. Ley, Solid State Commun. **39,** 625 (1981).
46 G. Polisski, D. Kovalev, G. Dollinger, T. Sulima, and F. Koch, Physica B: Condensed Matter **273–274,** 951 (1999).
47 P. T. B. Shaffer, Acta Crystallographica Section B: Structural Crystallography and Crystal Chemistry **25,** 477 (1969).
48 N. Begum, A. S. Bhatti, F. Jabeen, S. Rubini, and F. Martelli, J. Appl. Phys. **106,** 114317 (2009).
49 I. H. Campbell and P. M. Fauchet, Solid State Commun. **58,** 739 (1986).
50 T. V. Torchynska, A. V. Hernandez, A. D. Cano, S. Jiménez-Sandoval, S. Ostapenko, and M. Mynbaeva, J. Appl. Phys. **97,** 33507 (2005).
51 G. Polupan and T. V. Torchynska, Thin Solid Films **518,** S208 (2010).
52 T. V. Torchynska, A. D. Cano, S. J. Sandoval, M. Dybic, S. Ostapenko, and M. Mynbaeva, Microelectron. J. **36,** 536 (2005).
53 J. I. Langford and A. J. C. Wilson, J. Appl. Crystallogr. **11,** 102 (1978).
54 G. D. Mahan, R. Gupta, Q. Xiong, C. K. Adu, and P. C. Eklund, Physical Review B **68,** 073402 (2003).

55 T. Taguchi, T. Miyazaki, S. Iikubo, and K. Yamaguchi, Materials Science and Engineering: C **34,** 29 (2014).

56 S. Schelz and P. Oelhafen, Surf. Sci. **279,** 137 (1992).

57 X. L. Wu, S. J. Xiong, J. Zhu, J. Wang, J. C. Shen, and P. K. Chu, Nano Lett. **9,** 4053 (2009).

58 K. Shimoda, J.-S. Park, T. Hinoki, and A. Kohyama, Appl. Surf. Sci. **253,** 9450 (2007).

59 R. Alfonsetti, L. Lozzi, M. Passacantando, P. Picozzi, and S. Santucci, Appl. Surf. Sci. **70,** 222 (1993).

60 Y.-C. Yen, S.-C. Chao, H.-C. Wu, and N.-L. Wu, J. Electrochem. Soc. **156,** A95 (2009).

61 C. Das, M. Tallarida, and D. Schmeisser, Nanoscale **7,** 7726 (2015).

62 T. Takahagi and A. Ishitani, Carbon **22,** 43 (1984).

63 D. C. Marcano, D. V. Kosynkin, J. M. Berlin, A. Sinitskii, Z. Sun, A. Slesarev, L. B. Alemany, W. Lu, and J. M. Tour, ACS Nano **4,** 4806 (2010).

64 Y. Ma, H. Yang, J. Guo, C. Sathe, A. Agui, and J. Nordgren, Appl. Phys. Lett. **72,** 3353 (1998).

65 J. Bateman, R. Eagling, B. Horrocks, and D. Worrall, Chem. Commun., 2275 (1997).

66 D. Beke, Z. Szekrényes, I. Balogh, M. Veres, É. Fazakas, L. K. Varga, K. Kamarás, Z. Czigány, and A. Gali, Appl. Phys. Lett. **99,** 213108 (2011).

67 S. Limpijumnong, W. R. L. Lambrecht, S. N. Rashkeev, and B. Segall, Physical Review B **59,** 12890 (1999).

68 E. Biedermann, Solid State Commun. **3,** 343 (1965).

69 S. Zollner, J. G. Chen, E. Duda, T. Wetteroth, S. R. Wilson, and J. N. Hilfiker, J. Appl. Phys. **85,** 8353 (1999).

70 T. Dalibor, G. Pensl, H. Matsunami, T. Kimoto, W. J. Choyke, A. Schöner, and N. Nordell, physica status solidi (a) **162,** 199 (1997).

71 N. G. Wright, A. B. Horsfall, and K. Vassilevski, Mater. Today **11,** 16 (2008).

72 M. E. Levinshtein, S. L. Rumyantsev, and M. S. Shur, in *Properties of Advanced Semiconductor Materials: GaN, AIN, InN, BN, SiC, SiGe* (John Wiley & Sons, 2001), p. 96.

73 C. Persson and U. Lindefelt, J. Appl. Phys. **82,** 5496 (1997).

74 L. Brus, The Journal of Physical Chemistry **98,** 3575 (1994).

75 J. Zhu, Z. Liu, X. L. Wu, L. L. Xu, W. C. Zhang, and K. C. Paul, Nanotechnology **18,** 365603 (2007).

76 S. Yang, B. Kiraly, W. Y. Wang, S. Shang, B. Cao, H. Zeng, Y. Zhao, W. Li, Z.-K. Liu, W. Cai, and T. J. Huang, Adv. Mater. **24,** 5598 (2012).

77 D. Dai, N. Zhang, W. Zhang, and J. Fan, Nanoscale **4,** 3044 (2012).

78 Z. Szekrényes, B. Somogyi, D. Beke, G. Károlyházy, I. Balogh, K. Kamarás, and A. Gali, The Journal of Physical Chemistry C **118,** 19995 (2014).

79 D. Dai, X. Guo, and J. Fan, Appl. Phys. Lett. **106,** 053115 (2015).

80 A. Miranda and L. A. Pérez, Computational Materials Science **111,** 294 (2016).

81 M. Rashid, A. K. Tiwari, N. Wood, P. Briddon, J. P. Goss, M. J. Rayson, N. Wright, and A. B. Horsfall, in *Tuning Optoelectronic Properties of 4H-SiC QDs Using-H,-OH and-F Surface Functionalisation*, 2015 (Trans Tech Publ), p. 375.

82 M. Vörös, P. Deák, T. Frauenheim, and A. Gali, The Journal of Chemical Physics **133,** 064705 (2010).

83 M. V. Wolkin, J. Jorne, P. M. Fauchet, G. Allan, and C. Delerue, Phys. Rev. Lett. **82,** 197 (1999).

84 M. Rashid, A. K. Tiwari, J. P. Goss, M. J. Rayson, P. R. Briddon, and A. B. Horsfall, PCCP **18,** 21676 (2016).

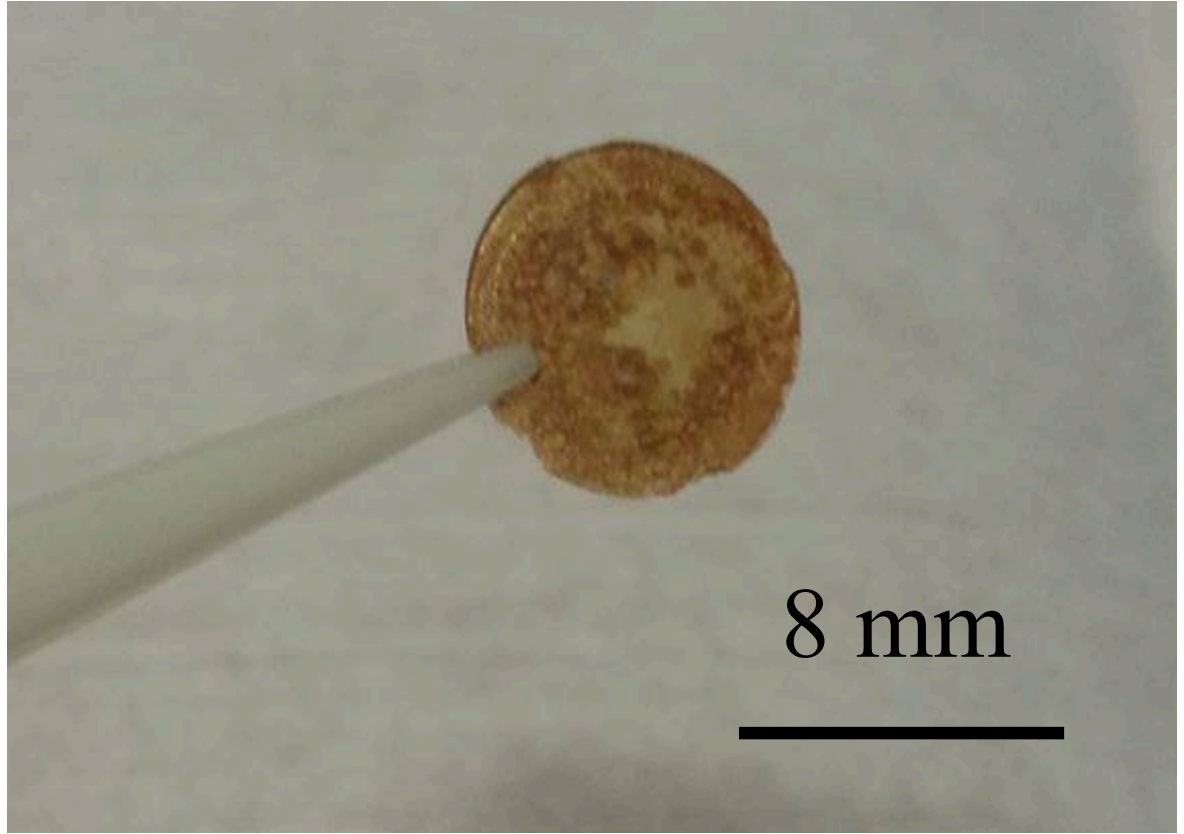
8 mm

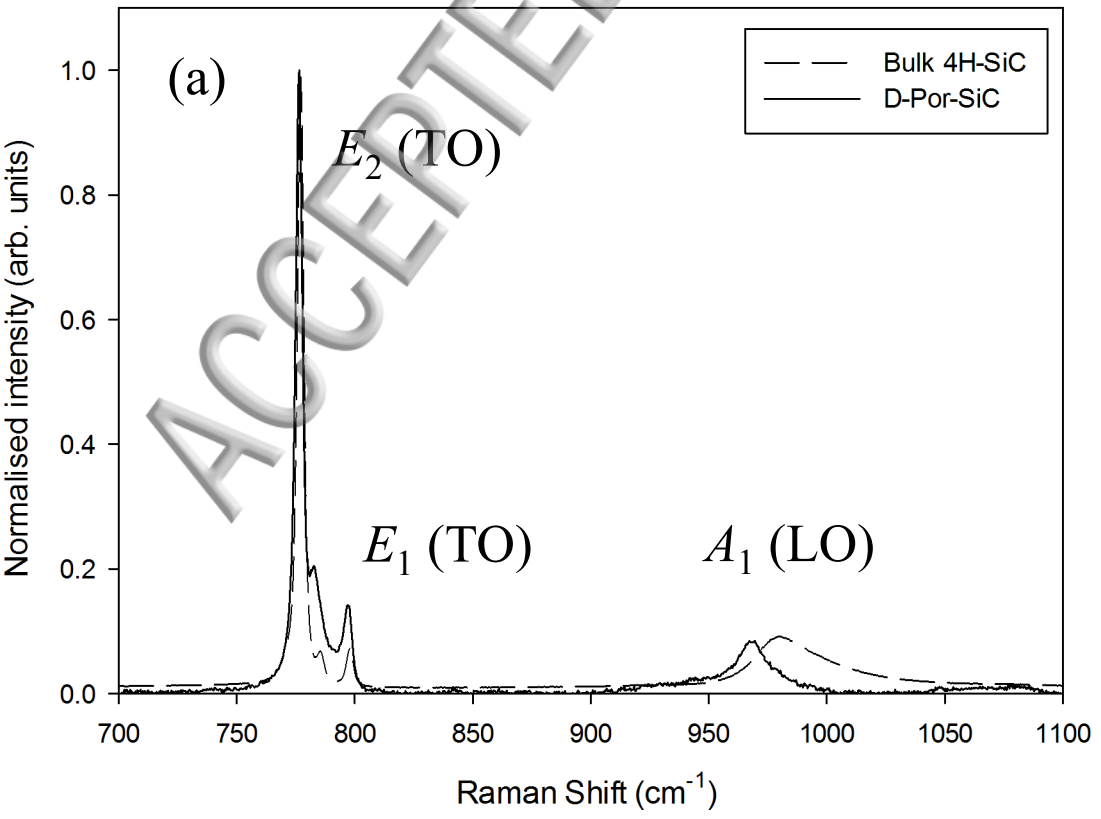
(a)
Bulk 4H-SiC
D-Por-SiC
E_2 (TO)
E_1 (TO)
A_1 (LO)
Normalised intensity (arb. units)
Raman Shift (cm^{-1})
0.0
0.2
0.4
0.6
0.8
1.0
700
750
800
850
900
950
1000
1050
1100

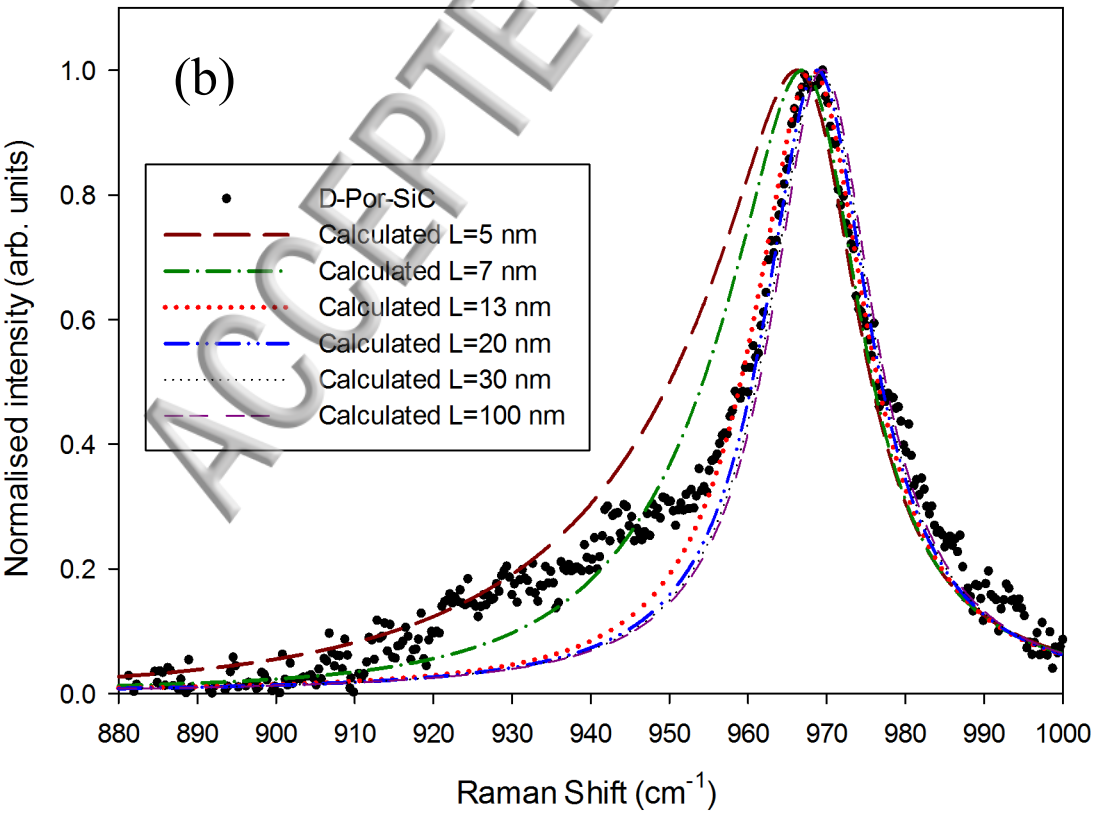
(b)
D-Por-SiC
Calculated L=5 nm
Calculated L=7 nm
Calculated L=13 nm
Calculated L=20 nm
Calculated L=30 nm
Calculated L=100 nm
Normalised intensity (arb. units)
Raman Shift (cm-1)
0.0
0.2
0.4
0.6
0.8
1.0
880
890
900
910
920
930
940
950
960
970
980
990
1000

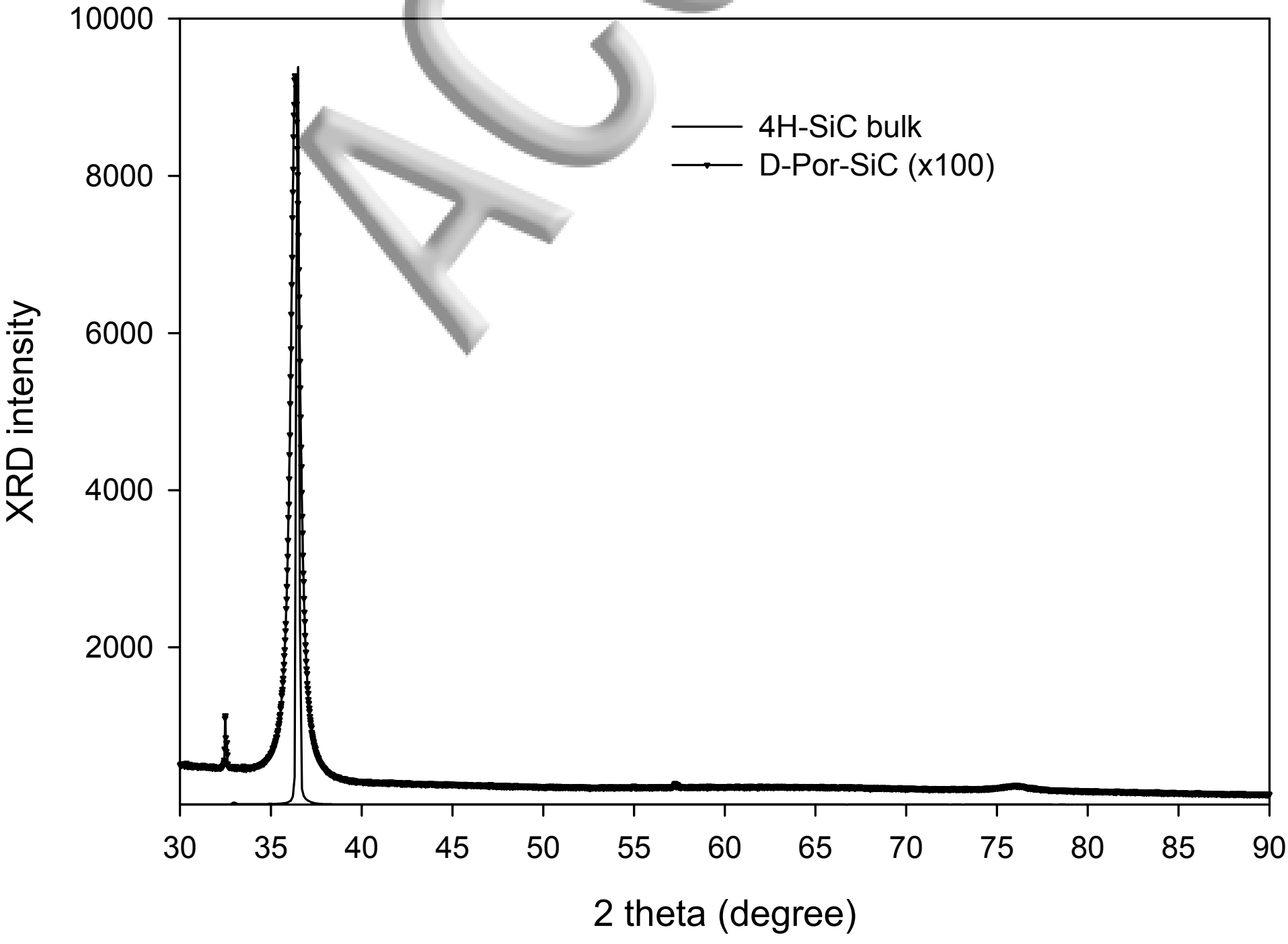
10000
8000
6000
4000
2000
XRD intensity
4H-SiC bulk
D-Por-SiC (x100)
30
35
40
45
50
55
60
65
70
75
80
85
90
2 theta (degree)

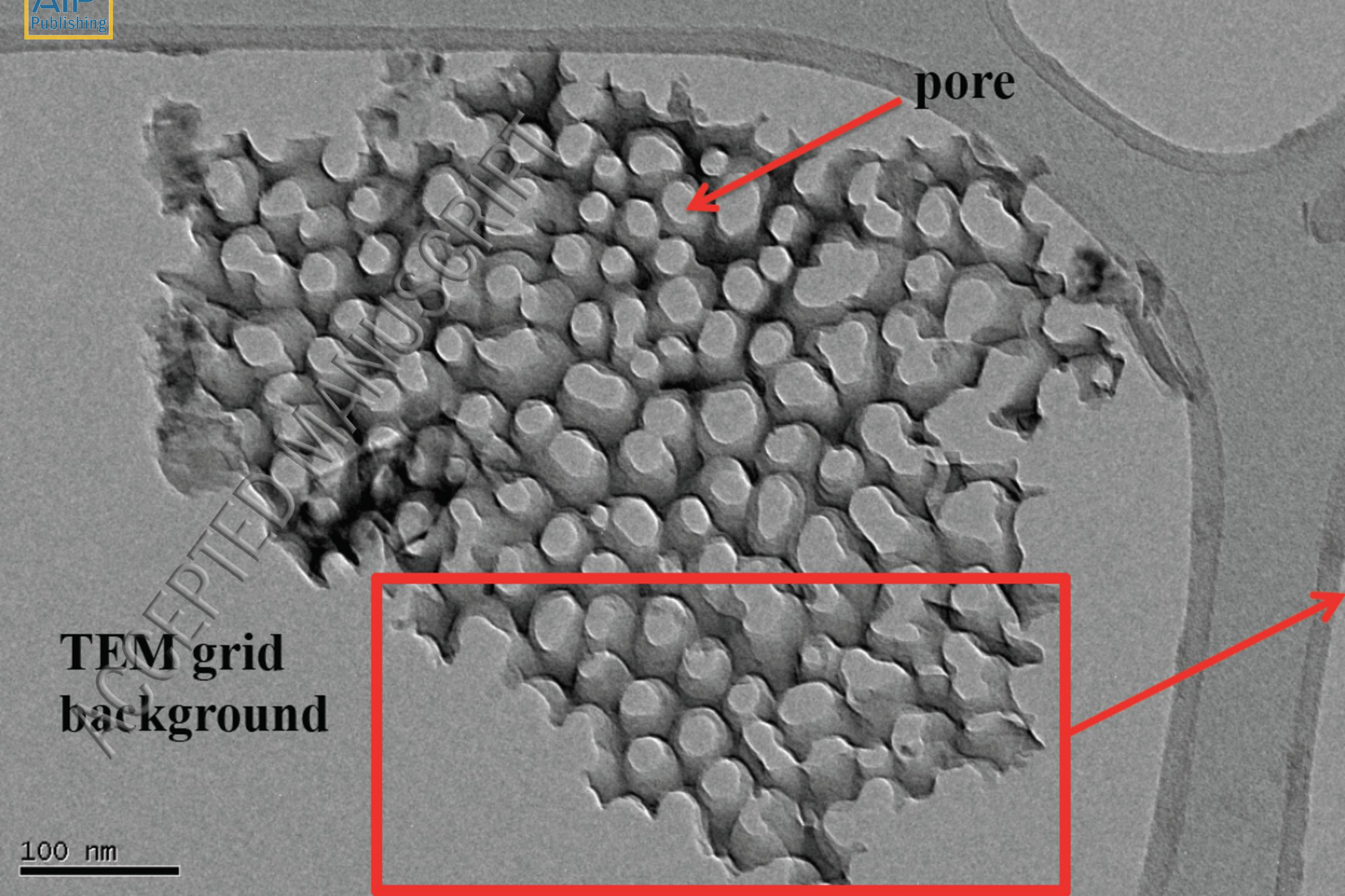

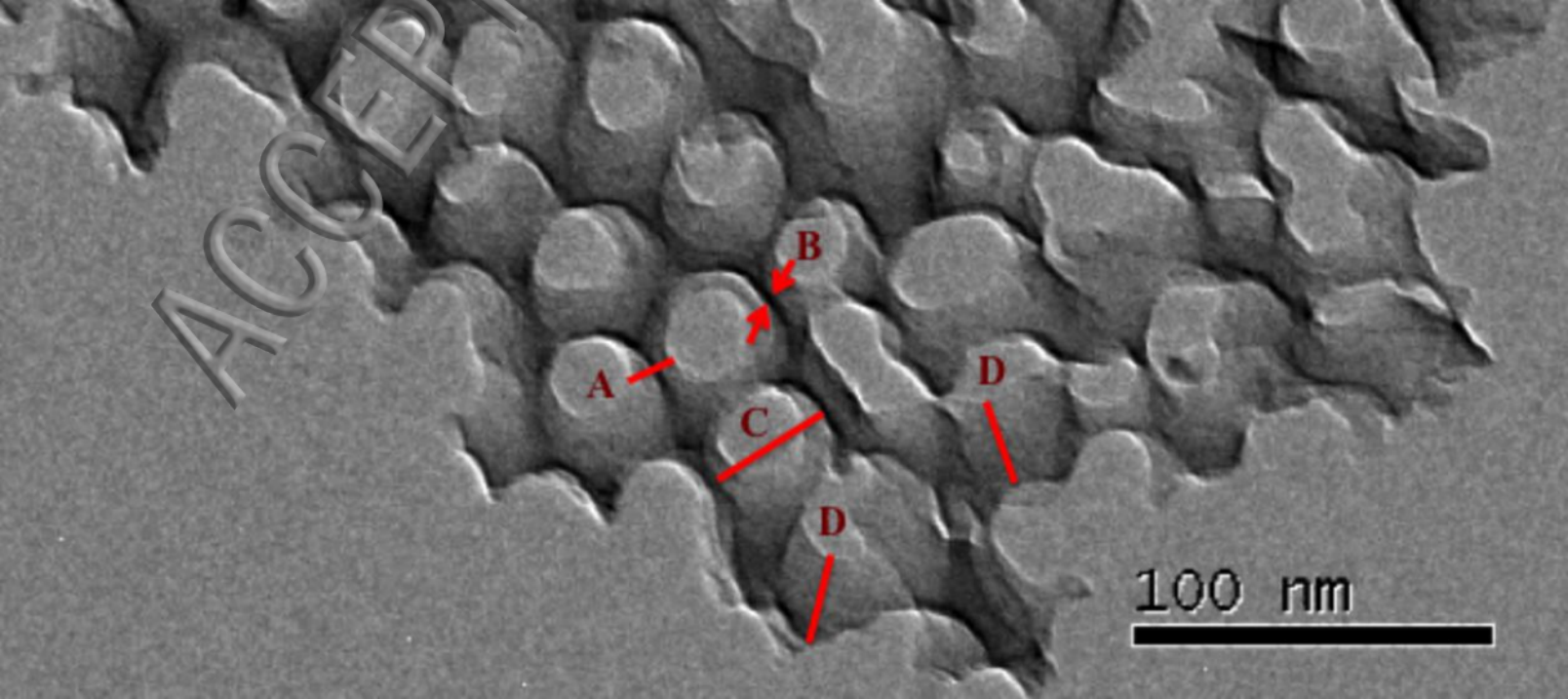
B
A
C
D
D
100 nm

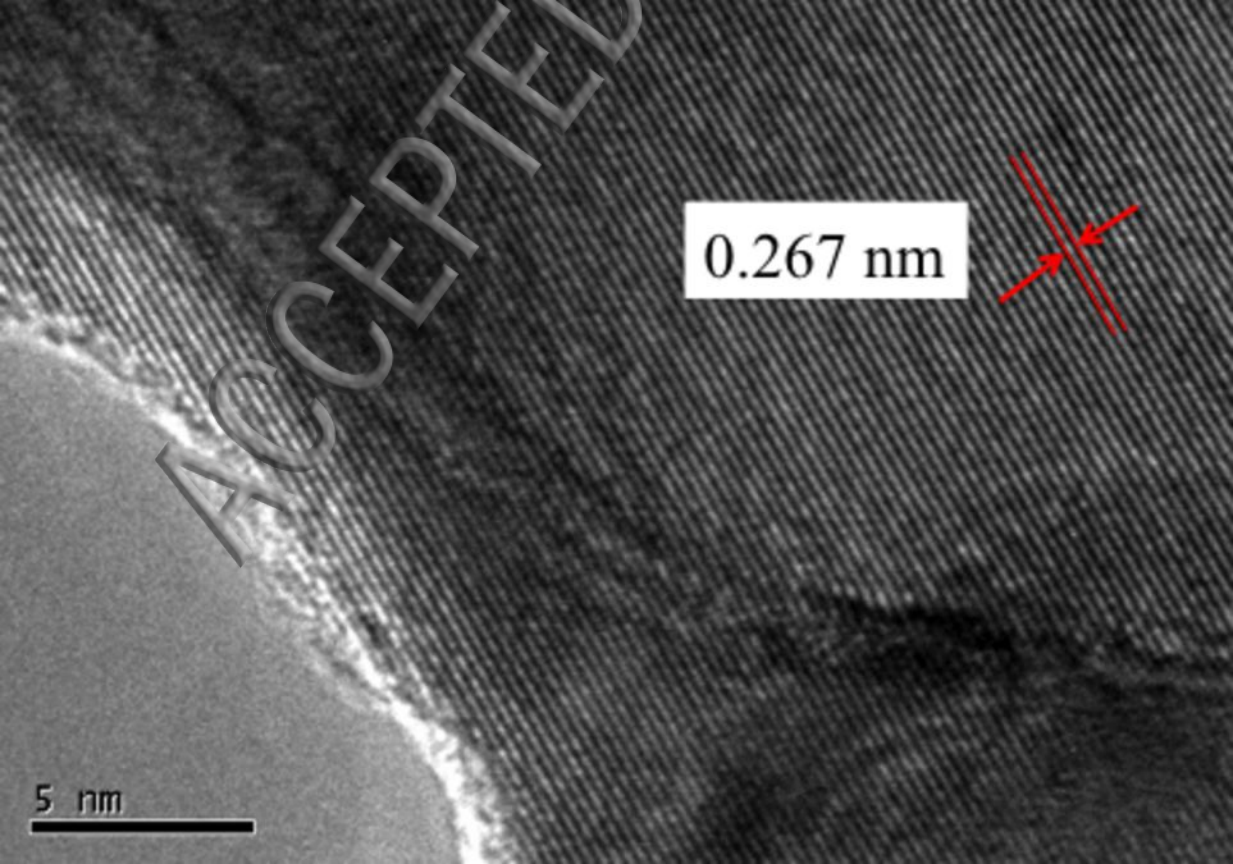

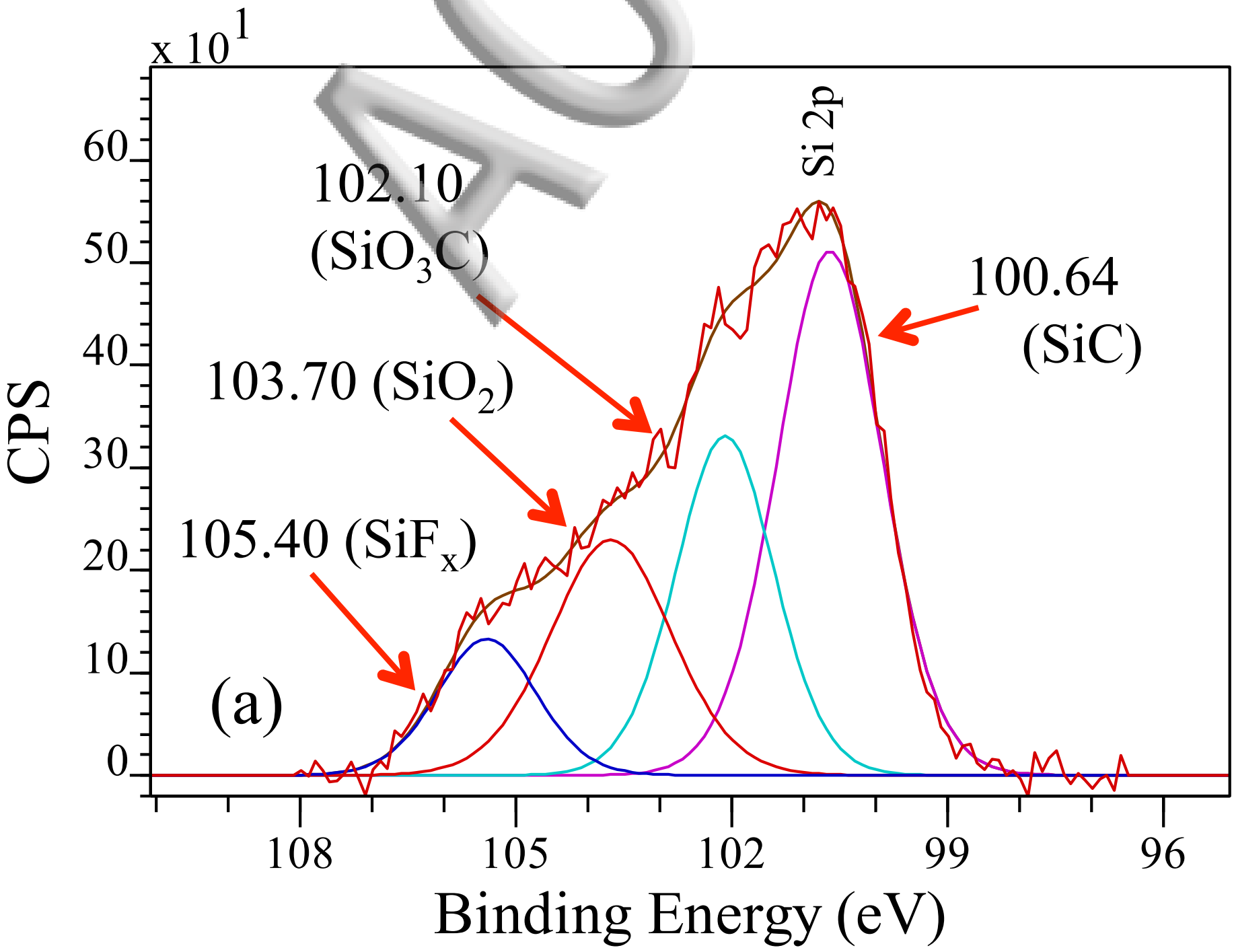
x 10^1
60
50
40
30
20
10
0
CPS
Si 2p
102.10
(SiO3C)
100.64
(SiC)
103.70 (SiO2)
105.40 (SiFx)
(a)
108
105
102
99
96
Binding Energy (eV)

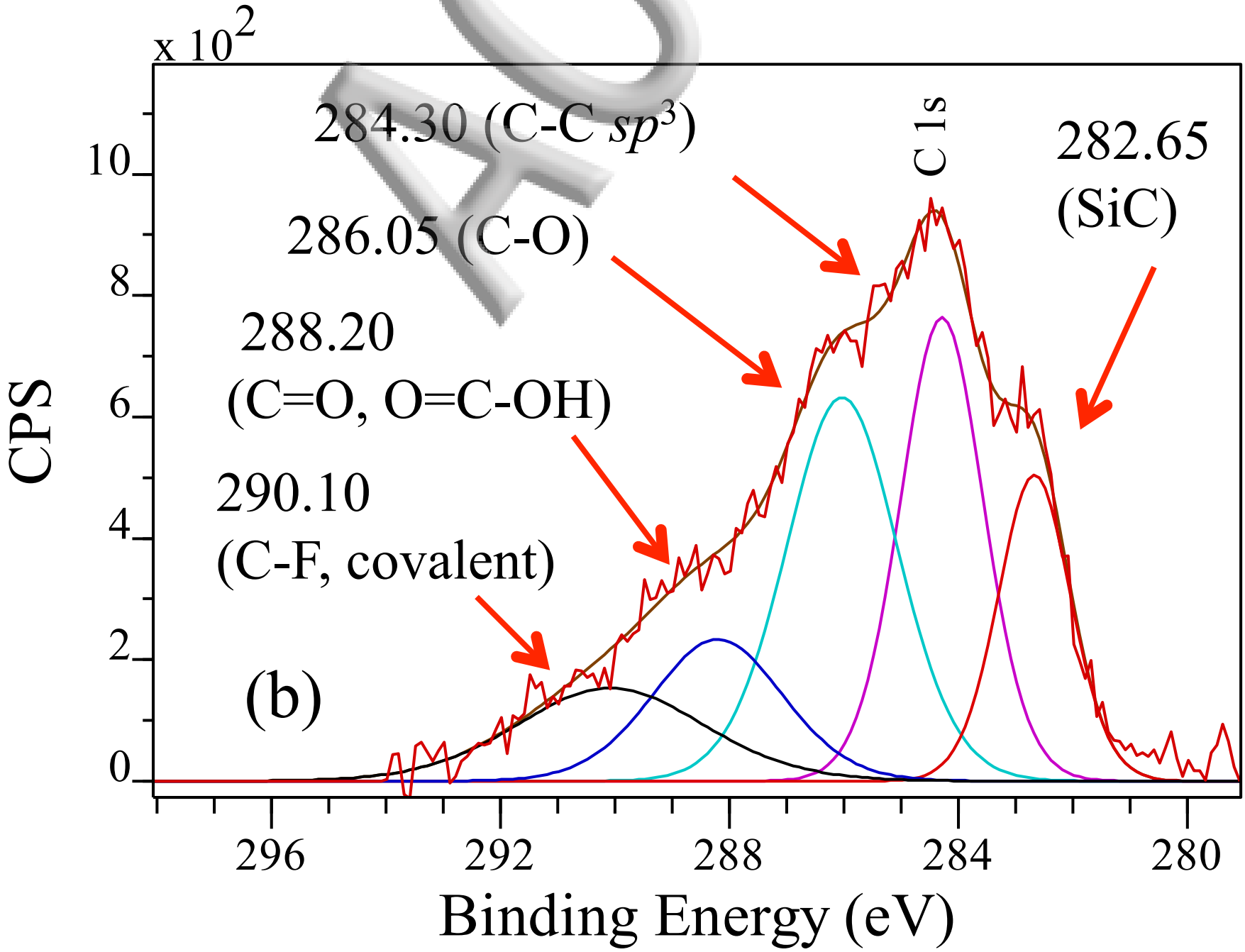
x 10^2
10
8
6
4
2
0
CPS
284.30 (C-C sp3)
286.05 (C-O)
288.20
(C=O, O=C-OH)
290.10
(C-F, covalent)
C 1s
282.65
(SiC)
(b)
296
292
288
284
280
Binding Energy (eV)

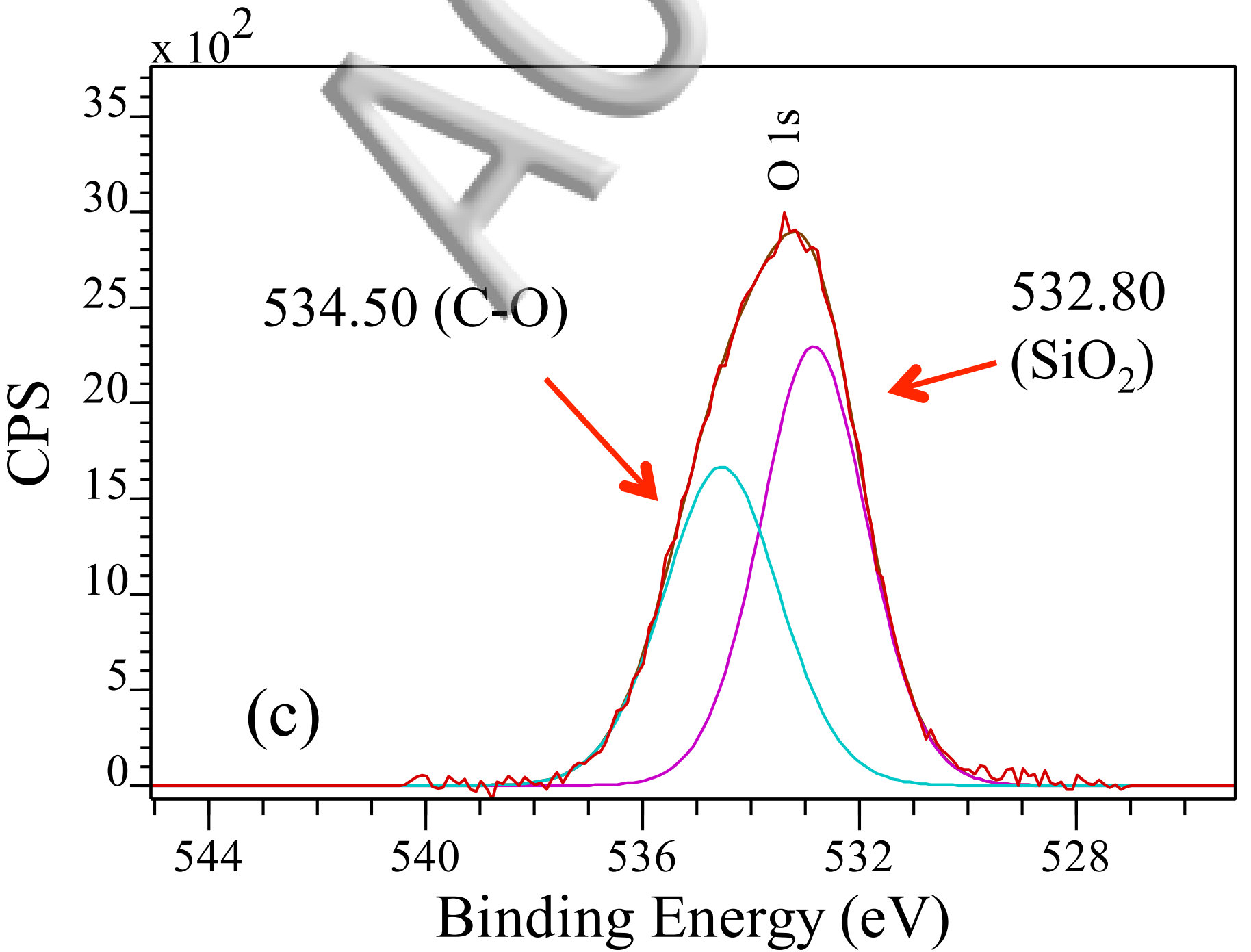
x 10^2
35
30
25
20
15
10
5
0
CPS
O 1s
534.50 (C-O)
532.80
(SiO2)
(c)
544
540
536
532
528
Binding Energy (eV)

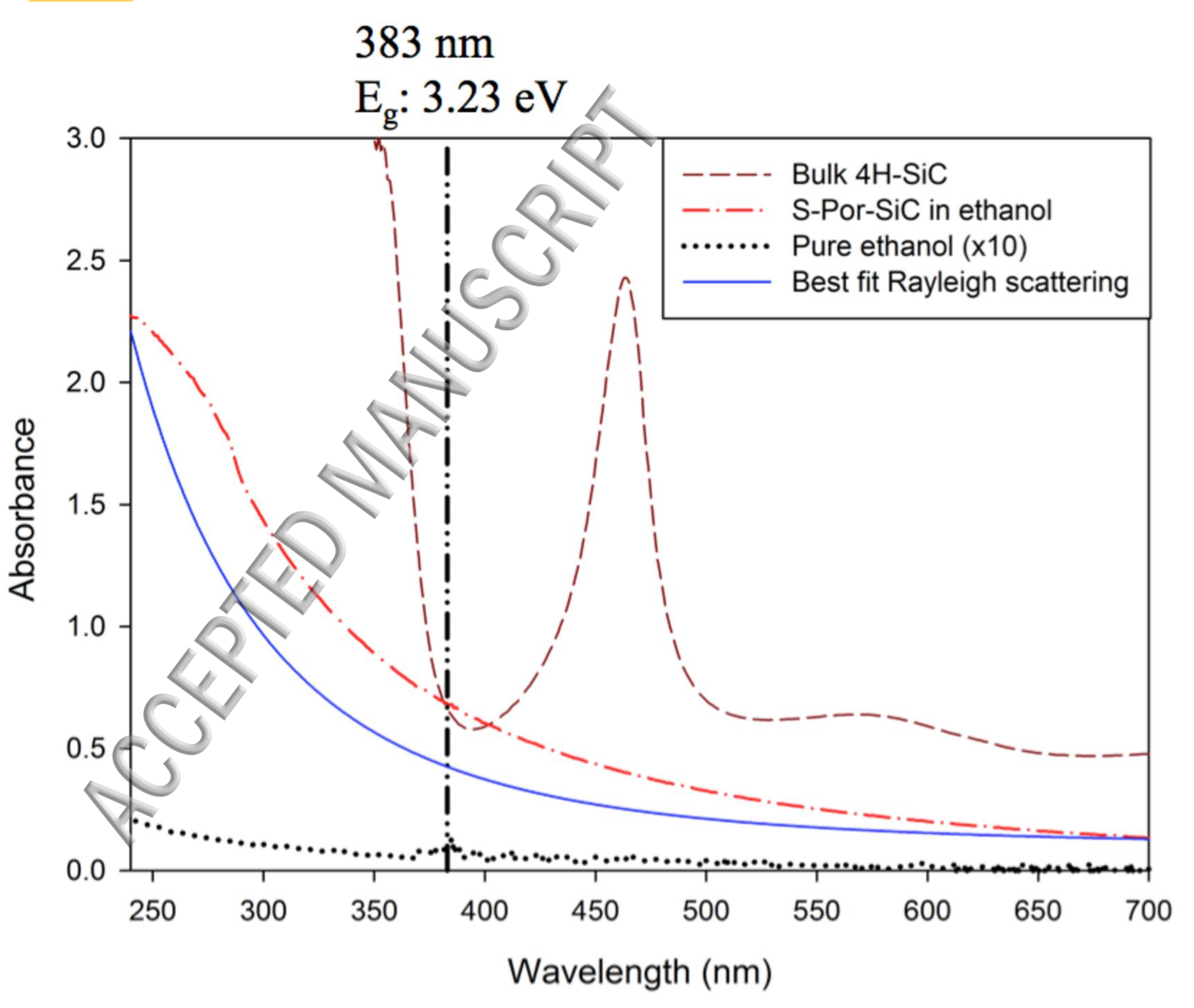

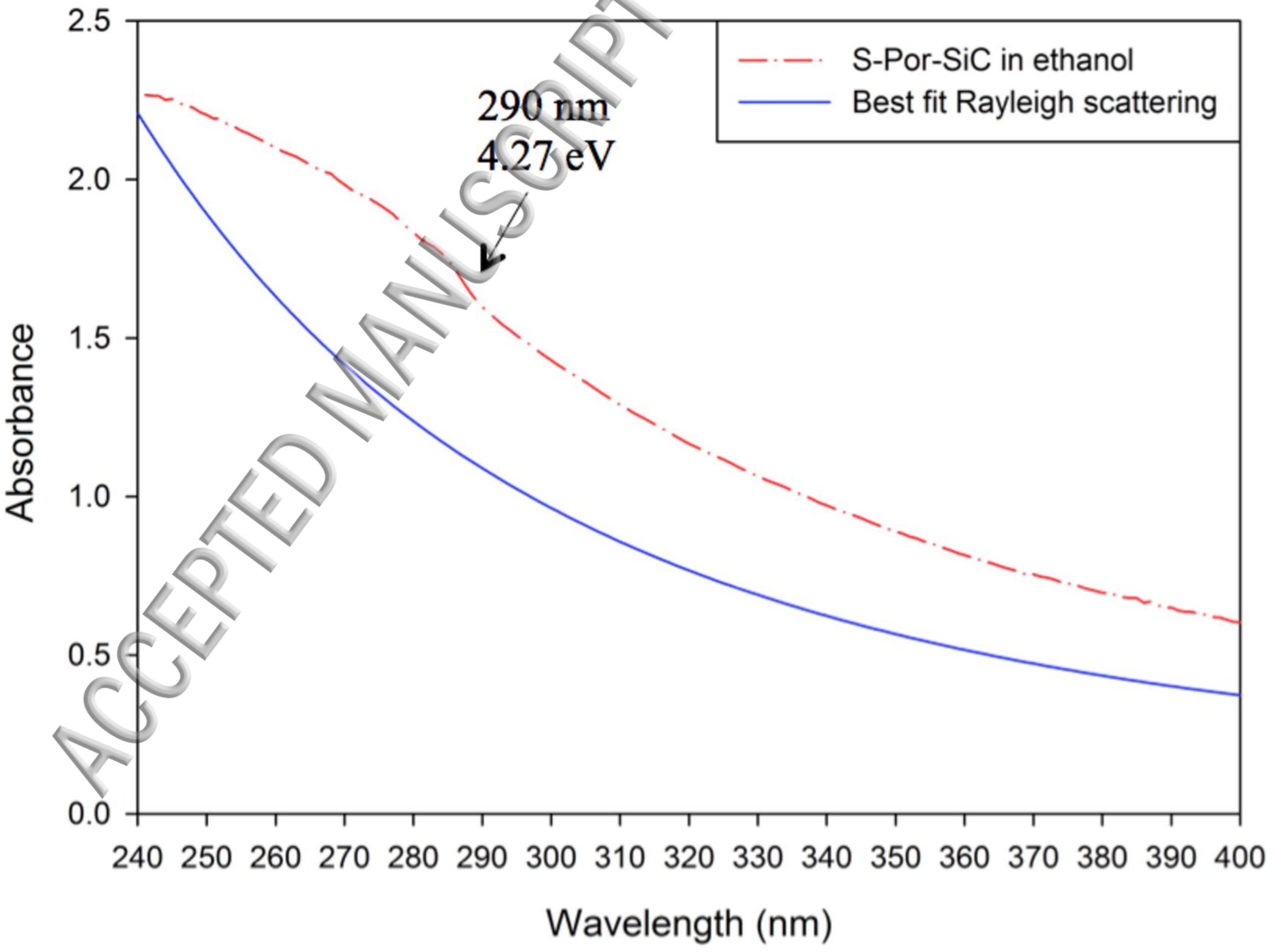

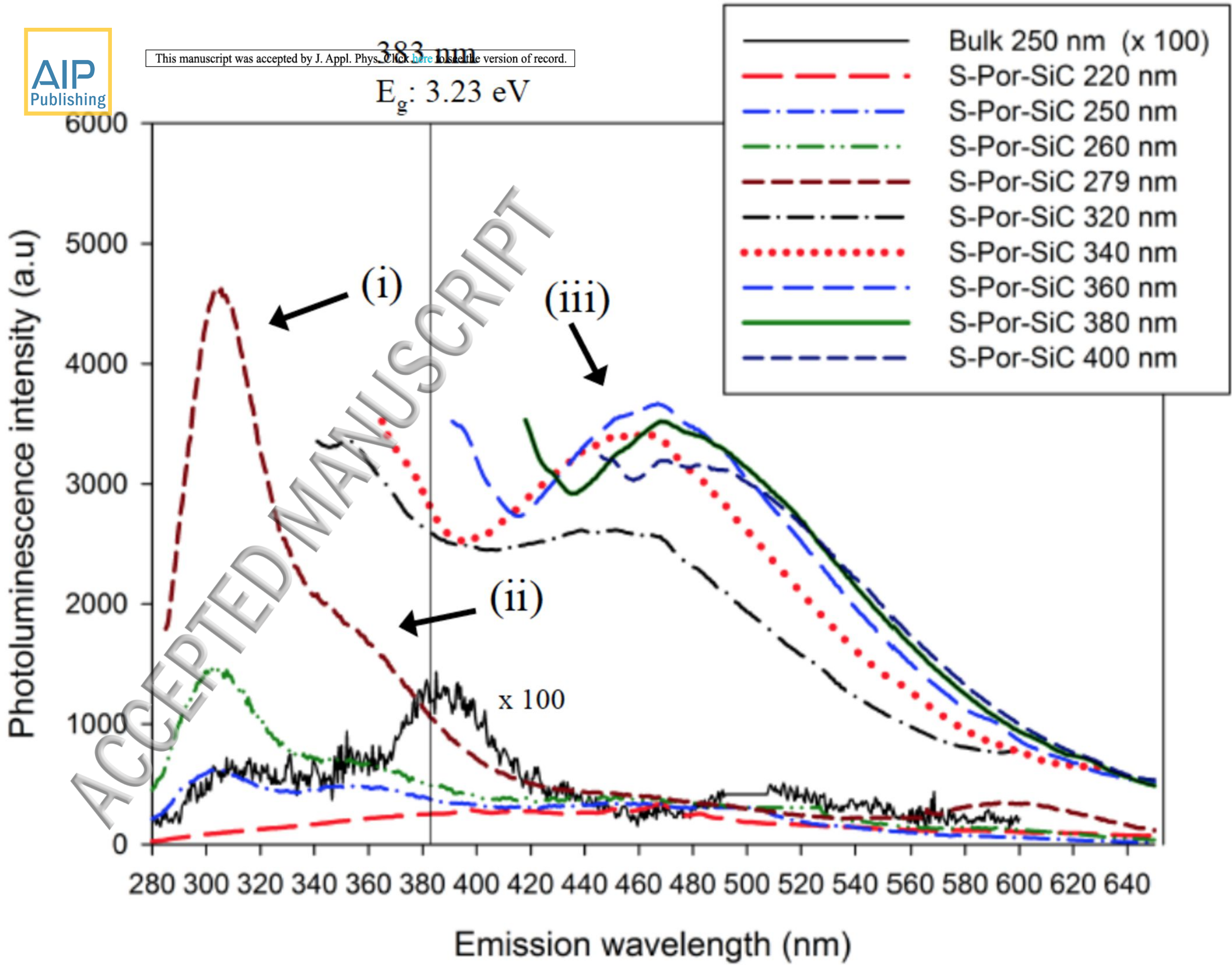

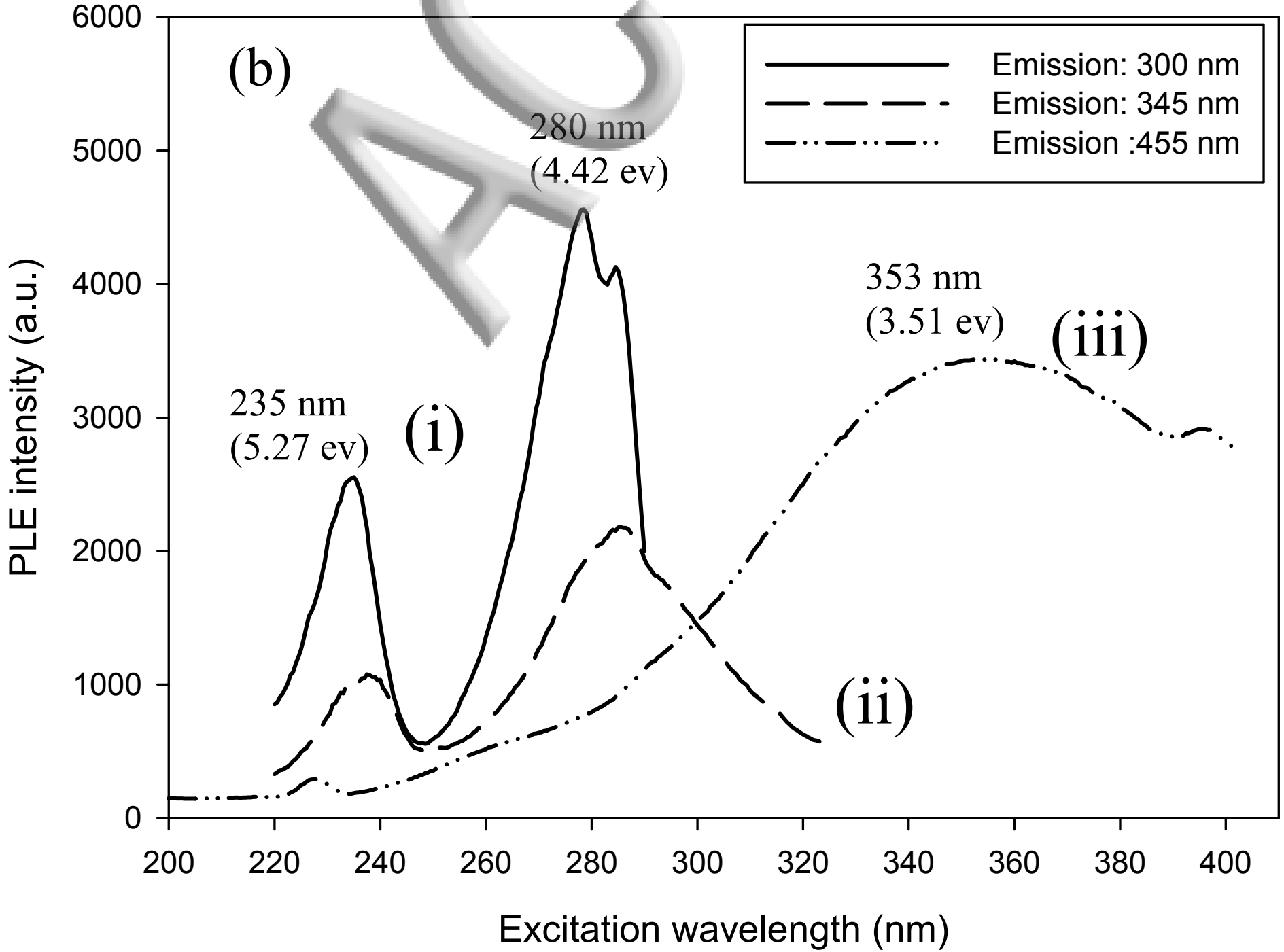
(b)
Emission: 300 nm
Emission: 345 nm
Emission :455 nm
280 nm
(4.42 ev)
353 nm
(3.51 ev)
235 nm
(5.27 ev)
(i)
(ii)
(iii)
PLE intensity (a.u.)
Excitation wavelength (nm)
0
1000
2000
3000
4000
5000
6000
200
220
240
260
280
300
320
340
360
380
400